

Testing Viability of Benchmark Dark Matter Models for the Galactic Center Excess

Yongao Hu¹, Cari Cesarotti^{1,2}, and Tracy R. Slatyer¹

¹*Center for Theoretical Physics – a Leinweber Institute, Massachusetts Institute of Technology, 77 Massachusetts Avenue, Cambridge, Massachusetts, USA*

²*Theoretical Physics Department, CERN, 1211 Geneva 23, Switzerland*

ABSTRACT: We examine the status of benchmark simplified dark matter models that have been proposed to explain the GeV gamma-ray Galactic Center excess. We constrain the available parameter space using updated observations from indirect detection, cosmology, direct detection, and accelerators. We show that there is still unconstrained parameter space in both classes of models we consider (a secluded dark sector with a vector portal coupling, and a two-Higgs doublet with a pseudoscalar mediator), and discuss the prospects for potential improvement of these constraints in future experiments.

Contents

1	Introduction	1
2	Dark matter models for the GCE	3
2.1	General considerations from the GCE rate and spectrum	3
2.2	Constraints from the cosmological history	5
2.3	Models	5
2.3.1	Secluded hypercharge model	6
2.3.2	Two-Higgs doublet model	8
3	Constraints	10
3.1	The secluded hypercharge model	11
3.1.1	Relic density calculation	11
3.1.2	Thermalization	12
3.1.3	CMB	14
3.1.4	Direct detection	15
3.1.5	Accelerator and beam dump experiments	16
3.1.6	Gamma-ray line search	16
3.1.7	Model variations	16
3.2	The 2HDM+ a model	17
3.2.1	Relic density calculation	17
3.2.2	Direct detection	17
3.2.3	Gamma-ray line search	19
3.2.4	B -physics	19
3.2.5	Invisible Higgs decay	20
3.2.6	Collider searches	21
4	Results	22
4.1	The secluded hypercharge model	23
4.2	The 2HDM+ a model	24
5	Future Projections	28
6	Conclusion	30
A	Calculation of the GCE spectra	33

1 Introduction

The origin of the Galactic Center excess (GCE) is a long-standing puzzle. First identified in 2009 by Goodenough and Hooper [1], the excess is spectrally broad with a peak around 1–3

GeV in energy, and spatially extended out to at least $10 - 20^\circ$ from the Galactic Center [2–4]. The signal is an “excess” in the sense that it cannot be readily absorbed into standard models of the diffuse Galactic gamma-ray emission arising from cosmic rays interacting with the gas and starlight (e.g. [5]). However, the inferred spatial and spectral properties of the GCE do inherit substantial uncertainties from the modeling of this background, and—in part for this reason—its physical origin remains unclear.

It is plausible that the GCE originates from familiar but uncatalogued sources, such as an unknown population of pulsars or other gamma-ray-emitting stars in the stellar bulge of the Milky Way [1, 6]. Some studies have suggested the detection of point-like structure in the GCE that would support this hypothesis (e.g. [7, 8]), or that detected gamma-ray sources might contribute significantly to the GCE (e.g. [9]). However, the initial searches for sources below Fermi’s detection threshold have been shown to be susceptible to false positives in the presence of background mismodeling [10, 11], and more recent studies with more sophisticated modeling and analysis techniques have generally found reduced or absent evidence for GCE-associated point sources compared to the initial claims [4, 12–15].¹ Perhaps the strongest argument for a pulsar (or other stellar) origin for the GCE is the claim that its morphology traces that of the Galactic stellar bulge (e.g. [16–19]). However, the robustness of this conclusion is disputed in the literature, with the preferred morphology depending to some degree on the modeling of the Galactic diffuse emission (e.g. [20–24]). A recent study has also argued that given the merger history of the Milky Way, a bulge-like morphology may be natural for a signal sourced from the dark matter (DM) halo, making it difficult to use morphological information to confirm or refute the pulsar hypothesis [25].

The GCE has garnered great interest from the particle physics community as a possible signal of new physics, notably DM annihilation. The GCE peaks at the Galactic Center and has an inferred spatial profile broadly consistent with expectations for the Milky Way’s DM halo from theory and simulations [26, 27] (subject to the uncertainties on both the predicted and inferred morphology described above). The annihilation cross section needed to fit the data is similar to that required to obtain the correct DM relic abundance through thermal freeze-out, albeit with substantial uncertainties [3, 28], and (within those uncertainties) remains broadly consistent with null results from gamma-ray observations of dwarf galaxies [29]. The spectrum is consistent with a range of Standard Model (SM) final states for the annihilation process (e.g. [3, 5, 30–32]), provided the DM mass is a few 10s of GeV or heavier. However, no counterpart signal has been observed in direct detection experiments or at particle accelerators; this significantly constrains the range of viable DM models for the excess.

This situation has prompted the community to broadly explore classes of DM models that could fit the GCE while evading other bounds (e.g. [32–41]). However, many of these analyses were done roughly a decade ago, based on the best limits available at that time; since then, direct detection limits have advanced by around 2 orders of magnitude [42, 43],

¹This does not exclude the pulsar hypothesis, as a sufficiently large population of dim pulsars would be indistinguishable from diffuse emission.

accelerators (including but not limited to the LHC) have collected much more data, and new analyses have been performed using updated cosmological and astrophysical datasets. Some of these analyses have claimed to set stringent limits on classes of models explaining the GCE, e.g. the gamma-ray line analysis of Ref. [44] constrains Higgs portal models. It is thus timely to reconsider the status of these scenarios, to better understand the plausibility (or otherwise) of the DM hypothesis for the GCE.

The outline of this work is as follows. We first introduce and summarize two major classes of benchmark simplified models proposed as viable DM scenarios for the GCE, and then discuss theoretical and observational tests of these scenarios.² In Section 2, we will discuss the DM models that can create the GCE signature. Section 3 will describe the various constraints on the DM models. Section 4 will report the updated results and the available parameter space in the DM models. Lastly, we will discuss the potential improvements on the constraints in future experiments in Section 5.

2 Dark matter models for the GCE

2.1 General considerations from the GCE rate and spectrum

There are significant uncertainties in the cross section required to fit the GCE [28], but smaller uncertainties in the cross section required to obtain the correct cosmological density of DM [45]. Given the similarity of the two cross sections (in the s -wave-dominated case) within the uncertainties [3, 28], we will focus in this work on models for the GCE that simultaneously obtain the correct relic density through the thermal freeze-out mechanism. Note that we do not claim this is the only viable mechanism or that our models represent an exhaustive set of possibilities. We focus on this scenario as a minimal solution to two outstanding questions in the SM phenomenology.

In this light, when we impose a cross section constraint, we require the DM annihilation cross section to be at the value required to match the thermal relic cross section ($\sim 4.4 \times 10^{-26} \text{ cm}^3 \text{ s}^{-1}$ for Dirac DM, corresponding to $\sim 2.2 \times 10^{-26} \text{ cm}^3 \text{ s}^{-1}$ for Majorana DM) [45, 46]. Further, the annihilation must be predominantly through an s -wave process at low velocity [32].

The spectrum of the GCE can be well described by scenarios where the DM annihilates to quarks that subsequently hadronize, and/or where cascade decays occur in the dark sector [31]. Hadronization (of quarks or gluons) generically produces neutral pions which decay to gamma-rays with a near-unity branching ratio and which can produce approximately the correct spectrum. The $b\bar{b}$ final state has often been used as a benchmark, but other final states with hadronic decays can also provide a good fit to the data [5, 31]. For scenarios of this type, the GCE is generally best fitted by DM particle candidates of 30-70 GeV in mass [32, 37, 40]. This will inform the mass range we consider. However, given the spectral uncertainties, we will not place a stringent prior on the branching ratios to different SM final states, provided there is a substantial branching ratio to hadronically decaying states [32, 47, 48]. We show some example spectra in Appendix A.

²We use $(+ - - -)$ as our metric choice. Unless otherwise specified, $\hbar = c = 1$.

We note that some papers have found good fits to the spectrum with an even wider range of final states. For example, Ref. [30] finds that DM masses up to 300 GeV can give an acceptable fit. Ref. [49] finds that a good fit is achieved for 60 GeV thermal relic DM annihilating to muons with a thermal relic cross section, once inverse Compton scattering of charged particles on the Galactic radiation field is included, and that scenarios of this type ameliorate tension with upper limits on the antiproton flux. Leptonic final states with a significant inverse Compton contribution are discussed more broadly in e.g. Ref. [50]. We will focus in this work on models where the DM mass is below 100 GeV and the final state is hadronic, but will comment briefly on these broader possibilities as appropriate.

In addition to the model-dependent constraints that will be the main focus of this work, there are tests of the DM hypothesis for the GCE that are nearly model-independent: in particular, searches for an identical counterpart signal in gamma-rays from dwarf galaxies. If we specify that the final state is comprised of quarks, this furthermore automatically implies a minimum flux of antiprotons from dark matter annihilation. While neither of these limits is truly model-independent (see e.g. [51] for an example of a class of models that evades bounds from dwarf galaxies) they are more generic than bounds from terrestrial experiments. Thus one might ask about the consistency of our broad requirements (DM mass below 100 GeV and hadronic final states) with these limits.

Current limits on hadronic final states from dwarf galaxy observations constrain cross sections comparable to those needed to fit the GCE [29]; for example, for 50-100 GeV DM annihilating to b quarks, the limit is in the range $1 - 2 \times 10^{-26} \text{ cm}^3/\text{s}$ for Majorana DM (which is slightly weaker than expected, but not to a degree that reflects a significant excess). There are prospects for improving the sensitivity of dwarf galaxy searches with either a successor gamma-ray instrument, or with the discovery of new dwarf galaxies whose locations can then be studied in archival data from the Fermi Gamma-Ray Space Telescope. We will keep the standard thermal relic cross section as our main benchmark but also discuss the impact on the allowed parameter space of a slightly smaller cross section, which would reduce tension with the dwarf limits.

There is a long-standing claim of a possible GCE counterpart signal in antiproton observations from AMS-02 (e.g. [52–54]), although the significance of that signal was found to be marginal by some later studies (e.g. [55, 56]). Ref. [49] found there is little evidence for an excess in more recent AMS-02 antiproton data [57], and that hadronic final states are in some tension with these newer data (preferring a cosmic-ray halo of smaller extent than favored by other cosmic-ray data). In the bulk of this work we will not focus on alleviating this tension, but we will briefly discuss variations on the secluded hypercharge model that could potentially achieve this goal.

Similarly, studies of the M31 (Andromeda) galaxy in the radio band have been used to set constraints on DM annihilation [58–61] (with one study claiming a possible GCE counterpart [62]), via searching for synchrotron emission from charged annihilation products diffusing in magnetic fields. Given the uncertainties in the diffusion modeling, these constraints do not yet seem to be in robust tension with the DM interpretation of the GCE [61].

2.2 Constraints from the cosmological history

In this paper, we consider the *freeze-out* model of DM production. The freeze-out mechanism assumes that in the radiation-dominated era, DM particles were in thermal equilibrium with SM particles until the DM annihilation rate dropped below the Hubble expansion rate; at that point the particles thermally decouple and the DM annihilation ‘freezes out’ [63].

The DM particle comoving density then roughly remains constant afterwards, resulting in what we term *thermal relics*, whose annihilation cross-section explains both the DM abundance and the GCE. Successful freeze-out (obtaining the observed relic density) constrains the interaction between DM and SM particles.

In this paper, we will denote this scenario as the *standard cosmological history* (also referred to as the “WIMP Next Door” in Ref. [64]). In particular, this assumption requires the coupling between the DM and SM sector to be large enough to fully equilibrate the two sectors prior to freeze-out. More complicated cosmological histories are also able to produce the thermal relic density [65, 66], but they might lead to a greater discrepancy between the cross sections required to match the observed density and to produce the GCE, and would require a more in-depth calculation; we do not consider such scenarios in this work.

2.3 Models

There are multiple classes of theories that can produce an excess of gamma-rays at GeV energies with features similar to the GCE. Based on the considerations above, we restrict our attention to models that (i) feature an *s*-wave annihilation channel which reproduces the thermal relics cross section $\langle\sigma v\rangle_{\text{th}} \simeq 4.4 \times 10^{-26} \text{ cm}^3\text{s}^{-1}$ (for Dirac DM), (ii) yield SM final states that hadronize or decay producing abundant photons, in order to reproduce the characteristic 1–3 GeV bump in the GCE for dark-matter masses near 30–70 GeV, and (iii) keep the dark and SM sectors in full thermal equilibrium until freeze-out, thereby fixing a minimal portal coupling. The final condition for viability is that the model features (iv) sufficient suppression of all other signals to evade the current bounds from indirect detection experiments, direct detection experiments, and from LHC searches; determining the remaining parameter space given these bounds will be the main focus of this work.

Over the past decade, the constraints in (iv) have become significantly more stringent. For example, one early work mapping out simplified models for the GCE [36] considered scenarios where the DM annihilates directly to SM particles through a mediator, and identified 16 distinct scenarios for the DM and mediator spins that could explain the GCE without violating constraints from colliders or direct detection. However, seven of those scenarios have now been excluded by updated direct-detection limits [43], at least in the regime assumed in Fig. 9 of that work;³ eight of the remaining nine scenarios correspond to scalar mediators, with the exception involving a vector mediator with axial-vector couplings to SM fermions. Thus recent improvements in terrestrial searches can certainly constrain

³This corresponds to taking the mediator mass to be significantly heavier than the DM mass, and the couplings of the mediator to the SM to be flavor-universal (+ proportional to the SM particle mass in the case of a scalar mediator) [67].

the space of possibilities for a DM origin of the GCE. At the same time, recent studies have identified models for the GCE that remain compatible with all constraints (e.g. for two very recent examples, see [68, 69]).

In this work, we update the status of two classes of models that are relatively simple, UV-complete, and were found to meet all requirements when they were first proposed as explanations for the GCE. One major class is the secluded dark sector, where the dark sector is coupled to the SM sector through a metastable mediator with a lower mass than the DM candidate [32, 34, 38]. As a result, secluded models can naturally evade both direct detection and collider production with an extremely small cross section [41], by reducing the coupling of the mediator to the SM without reducing the annihilation rate of the DM into mediators. One such minimal example on which we focus in this paper is *the secluded hypercharge model*, where a dark gauge boson of a $U(1)_D$ symmetry kinetically mixes with the gauge boson of the SM $U(1)_Y$ symmetry [32]. This model is the simplest UV-complete vector portal and has been well studied in the context of the GCE (e.g. [32, 34, 38, 70]).

The other model we consider is a two-Higgs doublet model (2HDM) with an additional pseudoscalar mediator that couples to a fermionic DM candidate (*the 2HDM+a model*). The 2HDM+a model is the minimal pseudoscalar portal that survives direct detection at one loop, making it of much interest in explaining the GCE [32, 37, 71]. Further, the 2HDM+a model is UV-complete, with an extended Higgs sector which is a common feature in beyond the Standard Model (BSM) models [72, 73] and well motivated by supersymmetry [74, 75]. It has also been discussed as a possible explanation for tentative hints in favor of a 95 GeV resonance at the LHC (e.g. [76]).

In the following sections, we will explain the calculation details of both the secluded hypercharge model and the 2HDM+a model.

2.3.1 Secluded hypercharge model

Here, we offer a review of the secluded hypercharge model. We consider an additional $U(1)_D$ symmetry. The particle content of this secluded sector is a heavy dark Dirac fermion χ (charged under $U(1)_D$) and a lighter vector mediator \hat{D} , which is the gauge boson of $U(1)_D$. The \hat{D} kinetically mixes with the gauge boson of $U(1)_Y$ with a mixing parameter ε [71, 77]:

$$\mathcal{L} \supset -\frac{1}{4}\hat{B}^{\mu\nu}\hat{B}_{\mu\nu} - \frac{1}{4}\hat{D}^{\mu\nu}\hat{D}_{\mu\nu} - \frac{\varepsilon}{2}\hat{D}^{\mu\nu}\hat{B}_{\mu\nu}, \quad (2.1)$$

where the $U(1)_Y$ field strength is $\hat{B}_{\mu\nu}$ and the $U(1)_D$ field strength is $\hat{D}_{\mu\nu}$.

We add a mass term for the dark gauge boson of mass \hat{m}_D :

$$\mathcal{L} \supset \frac{1}{2}\hat{m}_D^2\hat{D}^\mu\hat{D}_\mu. \quad (2.2)$$

We do not include a dynamical dark Higgs that gives mass to the \hat{D} in the model. If the \hat{D} gains its mass due to the Higgs mechanism, we assume that the dark Higgs has a higher mass than the dark gauge boson and the dark fermion, making it less relevant to the low-energy physics that is relevant to the GCE. It is also possible to give the \hat{D} a mass

through the Stückelberg mechanism, without invoking a dynamical dark Higgs [78]. Our results are largely insensitive to the mass-generating mechanism for the dark gauge boson (although a sufficiently light dark Higgs field would impact the phenomenology).

After the electroweak symmetry breaking, the neutral gauge sector contains $\hat{Z}_\mu = c_w \hat{W}_{3\mu} - s_w \hat{B}_\mu$ and \hat{D}_μ . We use the shorthand $c_a = \cos a$ and $s_a = \sin a$, and w the Weinberg angle. We can define the small mixing angle ξ and the auxiliary angle x with

$$\tan 2\xi = \frac{2\varepsilon s_w}{1 - \hat{m}_D^2/\hat{m}_Z^2}, \quad \sin x = \varepsilon. \quad (2.3)$$

Diagonalizing the mass matrix gives the physical masses of the gauge bosons Z and Z' [65, 71, 77]:

$$\begin{pmatrix} \hat{A} \\ \hat{Z} \\ \hat{D} \end{pmatrix} = \begin{pmatrix} 1 & -\frac{c_w s_x s_\xi}{c_x} & -\frac{c_w s_x c_\xi}{c_x} \\ 0 & c_\xi + \frac{s_w s_x s_\xi}{c_x} & \frac{s_w s_x c_\xi}{c_x} - s_\xi \\ 0 & \frac{s_\xi}{c_x} & \frac{c_\xi}{c_x} \end{pmatrix} \begin{pmatrix} A \\ Z \\ Z' \end{pmatrix}. \quad (2.4)$$

We can read off the physical masses as [71]:

$$m_A^2 = 0, \quad m_Z^2 = \hat{m}_Z^2 \left[1 + s_x^2 s_w^2 \left(1 + \frac{\hat{m}_D^2}{\hat{m}_Z^2} \right) \right], \quad m_{Z'}^2 = \hat{m}_D^2 (1 + s_x^2 c_w^2). \quad (2.5)$$

We can then obtain the covariant derivative [65, 77]:

$$\begin{aligned} D_\mu &\equiv \partial_\mu - i\hat{g}_D Q_D \hat{D}_\mu - ig_Y Q_Y \hat{B}_\mu - igT^a W_\mu^a \\ &= \partial_\mu - ieQA_\mu - igT^a W_\mu^a - i \left[e\varepsilon s_\xi Q + \frac{e}{s_w c_w} (c_\xi + \varepsilon s_w s_\xi) (T_3 - s_w^2 Q) + g_D Q_D s_\xi \right] Z_\mu \\ &\quad - i \left[e\varepsilon c_\xi Q + \frac{e}{s_w c_w} (s_\xi - \varepsilon s_w c_\xi) (T_3 - s_w^2 Q) + g_D Q_D c_\xi \right] Z'_\mu. \end{aligned} \quad (2.6)$$

where g_D is the coupling of Z' , Q_D is the dark charge, and $\hat{g}_D = g_D/\sqrt{1 - \varepsilon^2}$. For the SM parameters, g_Y is the hypercharge coupling constant, Q_Y is the hypercharge, e is the electric charge, g is the weak isospin coupling constant, and T^a labels the $SU(2)$ generators. Absorbing Q_D into g_D , we can then obtain the following interaction term for SM fermions ψ and the dark fermion χ [65, 71, 77]:

$$\begin{aligned} \mathcal{L} \supset & Z_\mu \left[\bar{\psi} \gamma^\mu \left(e\varepsilon s_\xi Q + \frac{e}{s_w c_w} (c_\xi + \varepsilon s_w s_\xi) (T_3 - s_w^2 Q) \right) \psi + \bar{\psi} \gamma^\mu \gamma^5 \left(\frac{e}{s_w c_w} (c_\xi + \varepsilon s_w s_\xi) T_3 \right) \psi \right] \\ & + Z'_\mu \left[\bar{\psi} \gamma^\mu \left(e\varepsilon c_\xi Q + \frac{e}{s_w c_w} (s_\xi - \varepsilon s_w c_\xi) (T_3 - s_w^2 Q) \right) \psi + \bar{\psi} \gamma^\mu \gamma^5 \left(\frac{e}{s_w c_w} (s_\xi - \varepsilon s_w c_\xi) T_3 \right) \psi \right] \\ & + A_\mu \left(eQ \bar{\psi} \gamma^\mu \psi \right) + g_D \left(Z_\mu s_\xi + Z'_\mu c_\xi \right) \bar{\chi} \gamma^\mu \chi. \end{aligned} \quad (2.7)$$

Summary of parameters in the secluded hypercharge model

There are four parameters in the secluded hypercharge model: the kinetic mixing parameter ε , the dark sector coupling g_D , the dark vector mediator mass $m_{Z'}$, and the dark fermion

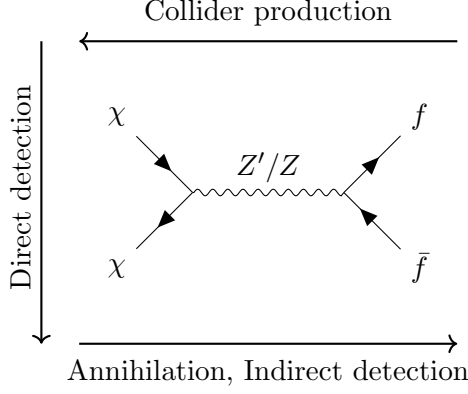


Figure 1. Feynman diagram illustrating χ interactions within the secluded hypercharge model. The process shows an s -channel annihilation into SM fermions, and the arrows indicate the relationship to collider production and direct detection.

mass m_χ . If we assume a standard cosmological history, g_D is determined by requiring that the annihilation produces the correct DM thermal relic density, and not independent [65] (a detailed discussion is offered in Section 3.1.1).

The parameter space we consider is:

- mass of the DM fermion $10 \text{ GeV} \leq m_\chi \leq 100 \text{ GeV}$ to produce the signature of the GCE,
- mass of the dark mediator $m_{Z'} < m_\chi$ at each m_χ to remain in the secluded regime,
- and kinetic mixing $10^{-9} \leq \varepsilon \leq 10^{-4}$ so that the cosmological history can remain standard (i.e. allowing the dark sector to reach equilibrium with the SM), while evading direct detection constraints.

2.3.2 Two-Higgs doublet model

Next, we offer a review on the two-Higgs doublet model. We consider an extended Higgs sector with two complex doublets (2HDM). The most general CP-conserving 2HDM potential is [37, 71]:

$$\begin{aligned}
 V(H_1, H_2)_{2\text{HDM}} = & \lambda_1 \left(H_1^\dagger H_1 - \frac{v_1^2}{2} \right)^2 + \lambda_2 \left(H_2^\dagger H_2 - \frac{v_2^2}{2} \right)^2 + \lambda_3 \left[\left(H_1^\dagger H_1 - \frac{v_1^2}{2} \right) + \left(H_2^\dagger H_2 - \frac{v_2^2}{2} \right) \right] \\
 & + \lambda_4 \left[\left(H_1^\dagger H_1 \right) \left(H_2^\dagger H_2 \right) - \left(H_1^\dagger H_2 \right) \left(H_2^\dagger H_1 \right) \right] + \lambda_5 \left[\text{Re} \left(H_1^\dagger H_2 \right) - \frac{v_1 v_2}{2} \right]^2 + \lambda_6 \left[\text{Im} \left(H_1^\dagger H_2 \right) \right]^2.
 \end{aligned}
 \tag{2.8}$$

where λ_a are the constants of the 2HDM, and v_i is the corresponding vacuum expectation value (vev) of each Higgs doublet H_i .

In unitary gauge we can write [37]

$$H_i = \frac{1}{\sqrt{2}} \begin{pmatrix} \sqrt{2}\phi_i^+ \\ v_i + \rho_i + i\eta_i \end{pmatrix}, \tag{2.9}$$

$$v_1^2 + v_2^2 = v_{\text{SM}}^2, \tag{2.10}$$

$$\tan \beta = \frac{v_2}{v_1}. \quad (2.11)$$

After symmetry breaking, we will have 5 physical states: CP-even h and H , CP-odd A , and charged H^\pm . We have a pair of neutral Higgs bosons with mixing parameter α ,

$$\begin{pmatrix} h \\ H \end{pmatrix} = \begin{pmatrix} -\sin \alpha & \cos \alpha \\ \cos \alpha & \sin \alpha \end{pmatrix}^{-1} \begin{pmatrix} \rho_1 \\ \rho_2 \end{pmatrix}, \quad (2.12)$$

a pseudoscalar boson,

$$A_0 = \sin \beta \eta_1 - \cos \beta \eta_2, \quad (2.13)$$

and a pair of charged Higgs bosons,

$$H^\pm = \sin \beta \phi_1^\pm - \cos \beta \phi_2^\pm. \quad (2.14)$$

2HDM with a pseudoscalar mediator (2HDM+ a)

To add a pseudoscalar portal for the GCE, we introduce a DM candidate Dirac fermion χ with mass m_χ coupled to a real singlet pseudoscalar mediator a_0 , which then couples to the SM by mixing with the pseudoscalar A_0 with mixing parameter B [79, 80]:

$$\mathcal{L}_D \supset g_\chi a_0 \bar{\chi} i \gamma^5 \chi, \quad (2.15)$$

$$V = V_{\text{2HDM}} + \frac{1}{2} m_{a_0}^2 a_0^2 + \frac{\lambda_a}{4} a_0^4 + i B a_0 H_1^\dagger H_2 + \text{h.c.} . \quad (2.16)$$

We assume \mathcal{L}_D and V are CP-conserving—thus a_0 does not have a vev, and we do not need to worry about large mass corrections or mixing of pseudoscalar and scalar mediators. We can define the mixing angle θ needed to rotate to the mass eigenstates A and a :

$$\begin{pmatrix} A_0 \\ a_0 \end{pmatrix} = \begin{pmatrix} \cos \theta & \sin \theta \\ -\sin \theta & \cos \theta \end{pmatrix} \begin{pmatrix} A \\ a \end{pmatrix}, \quad (2.17)$$

$$\tan 2\theta = \frac{2Bv_{\text{SM}}}{m_{A_0}^2/m_{a_0}^2}, \quad (2.18)$$

$$m_{a,A}^2 = \frac{1}{2} \left[m_{A_0}^2 + m_{a_0}^2 \pm \sqrt{(m_{A_0}^2 - m_{a_0}^2)^2 + 4B^2 v_{\text{SM}}^2} \right]. \quad (2.19)$$

The Lagrangian can then be simplified as:

$$V_{\text{port}} = \frac{1}{2v_{\text{SM}}} (m_A^2 - m_a^2) [\sin 4\theta a A + \sin^2 2\theta (A^2 - a^2)] [\sin(\beta - \alpha)h + \cos(\beta - \alpha)H], \quad (2.20)$$

$$\mathcal{L}_D \supset g_\chi (\cos \theta a + \sin \theta A) \bar{\chi} i \gamma^5 \chi. \quad (2.21)$$

The interaction vertices involving heavier SM fermions (t , b , and τ) are [80]:

$$\mathcal{L} \supset \sum_{f=t,b,\tau} \frac{m_f}{v_{\text{SM}}} \bar{f} [i \xi_f (\cos \theta A - \sin \theta a) \gamma_5] f. \quad (2.22)$$

There are multiple types of 2HDM models where down-type quarks, up-type quarks, and leptons couple to different doublets. In this paper, we consider the type-II 2HDM model, which yields similar Higgs sector phenomenology as the Minimally Supersymmetric Standard Model (MSSM) [75]. In the type-II 2HDM model, H_1 couples to down-type quarks and leptons while H_2 couples to up-type quarks [71, 80]:

$$\xi_t = \cot \beta, \quad \xi_b = \xi_\tau = \tan \beta. \quad (2.23)$$

In the type-II 2HDM model, $\tan \beta$, or the ratio between two vevs, controls the strength of coupling to down-type quarks compared to up-type quarks: the higher $\tan \beta$ is, the less the mediator couples to top quarks compared to bottom quarks and leptons.

To ensure that the light h boson acts as the SM Higgs boson to give the familiar behavior of the SM, and that the electroweak precision limit is met [81], we set $m_h \ll m_A = m_H = m_{H^\pm}$, and work in the decoupling limit $\cos(\beta - \alpha) = 0$ [82, 83]. Moreover, we set $m_a \ll m_A$, so that interactions involving the A mediator are suppressed at the lower energy scale relevant to the GCE. To keep the couplings perturbative, $m_A = m_H = m_{H^\pm} \leq \mathcal{O}(1 \text{ TeV})$ [80].

Summary of parameters in the 2HDM+ a model

Following the recommendation from the LHC Working Group [84], the list of parameters that we set are: $\lambda_1 = \lambda_2 = \lambda_3 = 3$, $m_h = 125 \text{ GeV}$, $v_{\text{SM}} = 246 \text{ GeV}$, $m_H = m_A = m_{H^\pm} = 800 \text{ GeV}$.

The parameters we vary are:

- the dark Dirac fermion mass $10 \text{ GeV} \leq m_\chi \leq 70 \text{ GeV}$ to facilitate matching the gamma-ray spectrum for the GCE,
- the light pseudoscalar mediator mass $m_a \leq 125 \text{ GeV}$,
- the ratio of the two vevs $5 \leq \tan \beta \leq 40$; we will see that at lower $\tan \beta$ values there are stringent indirect-detection limits, while at higher $\tan \beta$ the bottom and tau Yukawa interactions would start to become non-perturbative,
- the dark sector pseudoscalar coupling $0.5 \leq g_\chi \leq 1$ so that the DM sector remains perturbative while being able to reproduce the thermal relic density,
- and the mixing angle θ between pseudoscalar mediators A and a , with $10^{-3} \leq \theta \leq 1$, so that the relevant interactions remain perturbative and we are still able to reproduce the thermal relic density.

3 Constraints

Given the advancement in direct detection constraints, indirect detection constraints, and collider constraints over the last decade, let us now examine whether these models retain unconstrained phase space in the regime consistent with the GCE.

3.1 The secluded hypercharge model

3.1.1 Relic density calculation

First, we calculate the appropriate annihilation cross section to reproduce the thermal relic density. In the secluded regime, $\chi\bar{\chi} \rightarrow Z'Z'$ is the dominant annihilation channel (Fig. 2(a)).

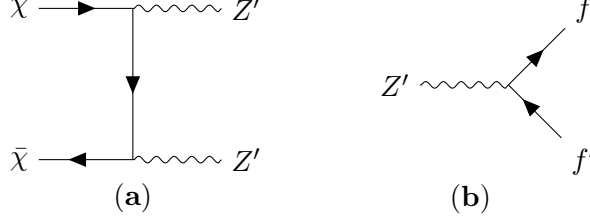


Figure 2. The processes to keep the equilibrium in early universe and achieving the relic abundance. (a): Dominant annihilation in dark sector in secluded regime $\chi\bar{\chi} \rightarrow Z'Z'$. (b): Decaying of dark boson back into the SM sector $Z' \rightarrow f\bar{f}$.

The s -wave thermally-averaged annihilation cross section is [65]

$$\langle\sigma v\rangle = \frac{g_D^4}{16\pi m_\chi^2} \frac{\left(1 - \frac{m_{Z'}^2}{m_\chi^2}\right)^{\frac{3}{2}}}{\left(1 - \frac{m_{Z'}^2}{2m_\chi^2}\right)^2}. \quad (3.1)$$

This expression is valid for $m_{Z'}/m_\chi \lesssim 0.95$ which covers most of our parameter space for the secluded regime. At $m_{Z'} \approx m_\chi$, velocity dependence becomes relevant and modifies the annihilation cross section (Eq. (3.1) is evaluated in the zero-velocity limit). Near threshold $m_{Z'} \rightarrow m_\chi$, the center-of-mass energy is approximately $s = 4m_\chi^2(1+v^2/4)$, so the final-state velocity becomes

$$\beta_f = \sqrt{1 - m_{Z'}^2/s} \simeq \sqrt{\Delta + v^2/4}, \quad (3.2)$$

with $\Delta \equiv 1 - m_{Z'}^2/m_\chi^2$. When $\Delta \rightarrow 0$, the phase-space factor no longer vanishes at finite velocity. Instead, $\beta_f \propto v$ and the s -wave cross section scales as $\langle\sigma v\rangle \propto v$.

Under a standard cosmological history, the WIMP thermally-averaged annihilation cross section for thermal relics if the DM candidate is a Majorana fermion for $m_\chi \geq 10$ GeV has to be [45]:

$$\langle\sigma v\rangle_{\text{Majorana}} \sim 2.2 \times 10^{-26} \text{ cm}^3\text{s}^{-1}. \quad (3.3)$$

For the dark Dirac fermion in our model, we need to double the annihilation cross section to reach the same thermal relic density [45]:

$$\langle\sigma v\rangle \sim 4.4 \times 10^{-26} \text{ cm}^3\text{s}^{-1} \approx 3.8 \times 10^{-9} \text{ GeV}^{-2}. \quad (3.4)$$

We can then calculate the dark sector coupling g_D as a function of m_χ and $m_{Z'}$. As we are assuming the Z' to stay in thermal equilibrium with the SM throughout freeze-out,

we can eliminate the Z' from the Boltzmann evolution equation, and effectively recover the standard calculation for the thermal relic density of the DM (the Z' is effectively just another field in the SM thermal bath). This argument does not rely on the Z' remaining relativistic, and so remains valid even for $m_{Z'}$ close to m_χ .

3.1.2 Thermalization

Next, we consider the constraint of the standard cosmological history. As the GCE requires models where $m_\chi > m_{Z'}$, the main decay process that we consider is $Z' \rightarrow f^+ f^-$ (Fig. 2(b)) to SM fermions f .

For the secluded hypercharge model, the tree level decay width of $Z' \rightarrow f \bar{f}$ is calculated to be [32, 71]:

$$\Gamma_{\text{HC, FO}} = \sum_f \frac{N_C^f m_D}{12\pi} \sqrt{1 - \frac{4m_f^2}{m_D^2}} \left[(g_V^f)^2 \left(1 + \frac{2m_f^2}{m_D^2} \right) + (g_A^f)^2 \left(1 - \frac{4m_f^2}{m_D^2} \right) \right]. \quad (3.5)$$

where N_C^f is the color factor of the SM fermion f , g_V^f is the vector coupling of fermion f with the Z' , and g_A^f is the axial vector coupling of fermion f with the Z' from (2.7).

In the standard cosmological history, the dark sector remains in equilibrium with the SM until the freeze-out temperature, which yields a lower bound for the kinetic mixing between the SM and DM sector. We estimate this by approximating the freeze-out temperature $T \sim m_\chi/20$ [71] to calculate the Hubble constant H at the freeze-out temperature in the radiation-dominated era [63]. The relativistic degrees of freedom g_* are taken as a function of temperature from [45], and we approximate the Hubble rate during radiation domination as:

$$H_{\text{FO}} = 1.66 g_*^{1/2} \frac{T_{\text{FO}}^2}{m_{\text{Pl}}}. \quad (3.6)$$

To ensure that the DM and the SM sector remain at equilibrium at freeze-out, we require that $\Gamma_{\text{HC, FO}} \geq H_{\text{FO}}$ and calculate the freeze-out temperature as a function of the kinetic mixing parameter ε . We then obtain a lower limit of ε for dark sector to remain in equilibrium in early universe. (This approach is similar to the estimate given in Ref. [41]; we obtain a somewhat weaker limit on ε than that work, possibly because we include more SM final states when computing the decay width.)

Refs. [64, 65] provide a more in-depth analysis of the cosmological history in the case of a light mediator, $m_{Z'} \lesssim 0.1 m_\chi$. Ref. [64] argued that for $T \gg m_{Z'}$, it is not the decay lifetime of the Z' that dominates the coupling to the SM, but instead $2 \rightarrow 2$ processes of the form $\text{SM SM} \rightarrow Z' \text{ SM}$. Ref. [65] pointed out more recently that in-medium effects suppress the Z' coupling to the SM for $T \gg m_{Z'}$, so in fact the dominant processes coupling the two sectors require the involvement of one or more DM particles; neglecting the direct interactions of Z' bosons with the SM, they find that full thermalization only occurs for significantly higher values of ε (compared to the result neglecting in-medium effects, where dark photon emission from the SM is important). Thus our $\Gamma_{\text{HC, FO}}$ -based estimate would underestimate the true thermalization bound on ε for $m_{Z'} \lesssim 0.1 m_\chi$, but for higher Z'

mass we do expect these decays (and their inverse decays) to dominate the energy transfer between the sectors, and our estimate should thus be valid. Furthermore, we find that the light-mediator region $m_{Z'} \lesssim 0.1m_\chi$ is already quite constrained by direct detection, in agreement with Ref. [65].

A more detailed calculation of the thermalization bound for $m_{Z'} \gtrsim 0.1m_\chi$ can be performed by solving the Boltzmann equations governing the number density and energy density of the two sectors. We neglect plasma effects because this regime corresponds to the Z' mass being larger than or equal to the temperature of the thermal bath around freezeout; a careful treatment of plasma effects would be needed to capture the transition to the light- Z' regime studied in Ref. [65], and might be an interesting direction for future work. We adapt the Boltzmann equations given in Ref. [85] to the case where $m_{Z'} < m_\chi$:

$$\frac{dn_\chi}{dt} + 3Hn_\chi = -\frac{1}{2}\langle\sigma v\rangle_{\chi\bar{\chi}\rightarrow Z'Z'}\left[n_\chi^2 - \frac{n_{\chi,0}(T')^2}{n_{Z',0}(T')^2}n_{Z'}^2\right] - \frac{1}{2}\langle\sigma v\rangle_{\chi\bar{\chi}\rightarrow f\bar{f}}[n_\chi^2 - n_{\chi,0}^2(T)] , \quad (3.7)$$

$$\frac{dn_{Z'}}{dt} + 3Hn_{Z'} = \frac{1}{2}\langle\sigma v\rangle_{\chi\bar{\chi}\rightarrow Z'Z'}\left[n_\chi^2 - \frac{n_{\chi,0}(T')^2}{n_{Z',0}(T')^2}n_{Z'}^2\right] - \Gamma(T')[n_{Z'} - n_{Z',0}(T)] , \quad (3.8)$$

$$\begin{aligned} \frac{d(\rho_\chi + \rho_{Z'})}{dt} + 3H(\rho_\chi + \rho_{Z'} + P_\chi + P_{Z'}) \\ = -\langle\sigma v\delta E\rangle_{\chi f\rightarrow\chi f}n_\chi n_f - m_{Z'}\Gamma(0)[n_{Z'} - n_{Z',0}(T)] - \frac{1}{2}m_\chi\langle\sigma v\rangle_{\chi\bar{\chi}\rightarrow f\bar{f}}[n_\chi^2 - n_{\chi,0}^2(T)] , \end{aligned} \quad (3.9)$$

As in that work, we take n_χ (ρ_χ , P_χ) to denote the total density (total energy density, total pressure) in $\chi + \bar{\chi}$; furthermore, we assume that the Z' and DM share a common temperature T' (which may differ from the SM temperature T), due to the lack of ε suppression in the relevant elastic scattering rates. 0 subscripts denote equilibrium densities (at zero chemical potential). Γ is the Z' decay rate to SM particles; at zero temperature, the rate $\Gamma(0)$ is given by Eq. 3.5. At higher temperatures, for $T' \lesssim m_{Z'}$, $\Gamma(T') = \Gamma(0)K_1(m_{Z'}/T)/K_2(m_{Z'}/T)$ [64] (here K_1 and K_2 denote modified Bessel functions of the 2nd kind).

Note that Ref. [85] uses the zero-temperature width in their Boltzmann equations. This is exact for the energy-density transfer equation (Eq. 3.9), because the suppression to the width for finite T' arises from time dilation, but the Z' total energy (and hence the energy transferred via decay) is enhanced by the same factor as the width is suppressed (i.e. the Lorentz γ factor). Thus the rate of energy transfer is simply $m_{Z'}\Gamma(0)$ independent of the temperature. However, in the number-density transfer equation, Γ should be evaluated at the dark-sector temperature T' (this distinction is important, as it ensures that fast decays separately drive $T' \rightarrow T$ and $n_{Z'} \rightarrow n_{Z',0}(T)$).

Relative to Ref. [85], we ignore processes that involve more than 2 particles in the initial state, since (unlike in that work) the leading 2-body processes are not kinematically suppressed. We do not include $2 \rightarrow 2$ scatterings between the Z' and the SM bath, because

while Ref. [64] argued that such scatterings should dominate over Z' decay for $T \gtrsim m_{Z'}$, Ref. [65] argued that in exactly this regime, the Z' should decouple from the SM due to plasma effects. We tested the effect of including elastic scattering between the DM and the SM bath (associated with the $\langle\sigma v\delta E\rangle$ term in Eq. 3.9, and computed as in Ref. [85]), which is the dominant mechanism equalizing the temperature of the sectors in the analysis of Ref. [65], but found that close to the thermalization floor, the effect of this term on the relic density is negligible (relative to the case where Z' decay is included but this term is not). We also tested the impact of omitting the DM annihilation directly to SM particles (controlled by $\langle\sigma v\rangle_{\chi\bar{\chi}\rightarrow f\bar{f}}$ in the equations above, and found that close to the thermalization floor the impact was negligible (due to the presence of the much stronger annihilation to $Z'Z'$).

We solve these equations down to a SM temperature of $T = m_\chi/200$, initially at a large value of $\varepsilon = 10^{-5}$, to establish the correct coupling $\alpha_D \equiv g_D^2/(4\pi)$ to obtain the desired relic density ($\Omega_c h^2 = 0.12$) in the fully-thermalized regime. (We compare this with the α_D value required to obtain a cross section of $\langle\sigma v\rangle = 4.4 \times 10^{-26} \text{ cm}^3/\text{s}$, and find good agreement.) We then lower ε while holding m_χ , $m_{Z'}$ and α_D fixed, and find the minimum value of ε such that (i) $d\ln(\Omega_c h^2)/d\ln\varepsilon < 0.2$ (i.e. the relic density is slowly varying with respect to ε), and (ii) changing the initial dark-sector abundances at $T = m_\chi$ by a large factor (specifically, between their equilibrium values and those values multiplied by a factor of e^{-5}) affects the final relic density by less than 1%, indicating that thermalization has erased information about the initial conditions. We then further confirmed that at these threshold values, the computed relic density matches the high- ε result (with the same α_D) to within 5% in all cases. The precise numerical thresholds used to define thermalization here are somewhat arbitrary, but changing them within reasonable bounds would only change the cutoff value of ε at the $\mathcal{O}(1)$ level.

3.1.3 CMB

The cosmic microwave background (CMB) is a relatively model-independent constraint on GCE models [86], directly constraining the annihilation cross section $\langle\sigma v\rangle$.

We use the updated CMB limit from the Planck Collaboration[65, 87]:

$$\frac{f_{\text{eff}} S_0 \langle\sigma v\rangle}{m_\chi} < 14 \times 10^{-28} \text{ cm}^3 \text{ s}^{-1} \text{ GeV}^{-1}, \quad (3.10)$$

where f_{eff} is the efficiency factor, and S_0 is the Sommerfeld enhancement.

The efficiency factor f_{eff} can be calculated from the individual efficiency factors for different decay channels of Z' [65]:

$$f_{\text{eff}}^{\text{net}} = \sum_{\ell} \text{Br}(Z' \rightarrow \ell\ell) f_{\text{eff}}^{VV\rightarrow 4\ell}(m_\chi) + \sum_{X \neq \ell} \text{Br}(Z' \rightarrow X X) f_{\text{eff}}^{XX}\left(\frac{m_\chi}{2}\right). \quad (3.11)$$

We obtain the Z' branching ratio from Ref. [88] and the individual f_{eff} factors from Ref. [89].

We estimate the Sommerfeld enhancement S_0 to the cross section, significant when $m_{Z'} \ll m_\chi$, using the analytic solution for the Hulthén potential [65, 90, 91]:

$$S_0(g_D, r, v) = \frac{g_D^2}{2v} \frac{\sinh\left(\frac{6v}{\pi r}\right)}{\cosh\left(\frac{6v}{\pi r}\right) - \cosh\left(\sqrt{\left(\frac{6v}{\pi r}\right)^2 - \frac{24\alpha_D}{r}}\right)}, \quad (3.12)$$

where $r = m_{Z'}/m_\chi$, and v is the velocity of the DM at the CMB epoch v_{CMB} , which can be in the range of $\sim 10^{-5}$ to $\sim 10^{-11}$ [65]. Note that the precise value of v_{CMB} does not affect the calculation because in our parameter space, $r \gg v_{\text{CMB}}$, and the Sommerfeld enhancement is “saturated” (i.e. velocity-independent) for the vast majority of parameter space apart from the few very fine-tuned regions at the tips of the resonance peaks.

3.1.4 Direct detection

Direct detection experiments constrain high kinetic mixing ε as they are sensitive to the process $\chi f \rightarrow \chi f$ (Fig. 3).

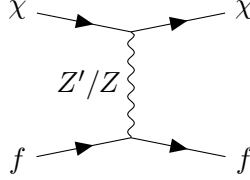


Figure 3. The direct detection process of $\chi f \rightarrow \chi f$ in the secluded hypercharge model.

At $m_{Z'}/m_\chi \gtrsim 0.01$, the effect of recoil energy on the DM-nucleon scattering is negligible [65]. We can then calculate the direct detection cross section of DM-nucleon scattering for the secluded hypercharge model [34, 65]:

$$\sigma_N = \frac{\mu_{\chi N}^2}{\pi} \left[\sum_{i=Z, Z'} V_{\chi, i} \frac{Z_N (2V_{u, i} + V_{d, i}) + (A_N - Z_N) (V_{u, i} + 2V_{d, i})}{A_N m_i^2} \right]^2, \quad (3.13)$$

$$\approx 1.67 \times 10^{-30} \text{ cm}^2 g_D^2 \varepsilon^2 (m_{Z'}/\text{GeV})^{-4}$$

where in the 2nd line we have assumed $m_D \ll m_Z$, $m_\chi \gg m_N$, and $\epsilon \ll 1$, and we use the full expression in the 1st line when computing our constraints. Here A_N is the mass number, Z_N is the atomic number, $m_N \approx 0.939$ GeV is the mass of nucleon, $\mu_{\chi N} = m_\chi m_N / (m_\chi + m_N)$ is the reduced mass, and the vector couplings

$$V_{q, Z} = e \varepsilon s_\xi Q_q + \frac{e}{s_w c_w} (c_\xi + \varepsilon s_w s_\xi) (T_{3, q} - s_w^2 Q_q), \quad (3.14)$$

$$V_{q, Z'} = e \varepsilon c_\xi Q_q + \frac{e}{s_w c_w} (s_\xi - \varepsilon s_w c_\xi) (T_{3, q} - s_w^2 Q_q), \quad (3.15)$$

$$V_{\chi, Z} = g_D s_\xi, \quad (3.16)$$

$$V_{\chi, Z'} = g_D c_\xi, \quad (3.17)$$

where $q = u, d$.

We will compare this to the updated LUX-ZEPLIN result [43].

3.1.5 Accelerator and beam dump experiments

In high intensity experiments, Z' can be produced and detected through their visible decays into the SM charged particles (we are never in the regime where the Z' decays invisibly into the dark sector, because of our condition that $m_\chi > m_{Z'}$). Accelerator and beam dump experiments, including e^+e^- colliders, the LHC, beam dump experiments, and meson factories, thus provide exclusion limits for the kinetic mixing parameter ε against the mass of the dark mediator $m_{Z'}$. We obtain the updated limits on the Z' parameter space from [92].

3.1.6 Gamma-ray line search

We can also consider the gamma-ray line search using data from the Fermi Gamma-Ray Space Telescope experiment [44], which tightly constrains processes producing mono-energetic gamma-ray photons. In the secluded hypercharge model, an on-shell Z' boson cannot decay into two on-shell photons by the Landau-Yang theorem [93]. In the narrow regime with $m_Z < m_{Z'} < m_\chi \leq 100$ GeV, the on-shell Z' can potentially decay into $Z + \gamma$. In this case, the branching ratio for the decay Z' into $Z + \gamma$ is loop-suppressed. This does not, however, necessarily render the gamma-ray line constraint irrelevant, since the line-search limits can be about 2 – 3 orders of magnitude stronger than those from the continuum. That said, in this on-shell decay regime, broadening of the signal into a box spectrum weakens the line-search sensitivity. The photon will also be lower-energy than in the $\gamma\gamma$ case, meaning the relevant backgrounds are higher and the sensitivity is lower. Moreover, following Ref. [94], we estimate the branching ratio to be lower than $\sim 10^{-4}$, which leaves the process unconstrained by the gamma-ray line search.

Outside this regime, for $m_{Z'} < m_Z$, we only need to consider processes with the DM candidate χ in the initial state. All such processes involving direct annihilation to SM particles, including $\gamma + X$ [94], are suppressed by a factor of ε^2 relative to the $\bar{\chi}\chi \rightarrow Z'Z'$ annihilation that sources the continuum spectrum, and thus are expected to be negligible for the parameter space allowed by other constraints (which we will find require $\varepsilon \lesssim 10^{-4}$).

3.1.7 Model variations

The limits discussed for the secluded hypercharge model would broadly generalize to other secluded models with a vector mediator associated with the $U(1)$ symmetry such as the $B-L$ portal, the Baryon portal, and the L_i-L_j portal, in which we gauge baryon number minus lepton number, the baryon number, and the difference of two lepton families respectively [32]. To obtain the limits in these models, we would need to adjust the couplings g_V^f and g_A^f between the SM fermion f and the dark gauge boson Z' from the secluded hypercharge model.

If a non-hadronic final state is desired (e.g. to avoid constraints from antiprotons as in Ref. [49]), this might favor scenarios where the Z' kinetically mixes with the gauge boson corresponding to the difference of two lepton families, in particular $L_e - L_\mu$ or $L_\mu - L_\tau$. Ref. [49] identifies muon-rich final states as the preferred channel (for a DM mass around 60 GeV and a thermal relic cross section). In the $L_\mu - L_\tau$ case, if the Z' is lighter than

$2m_\tau \approx 3.5$ GeV, annihilations will be essentially entirely to muons; this setup would also alleviate direct-detection constraints due to the mediator's lack of a direct coupling to quarks and gluons. Ref. [68] studies such leptophilic models for the GCE and finds that the $L_\mu - L_e$ model is particularly favorable.

3.2 The 2HDM+ a model

3.2.1 Relic density calculation

First, for the 2HDM+ a model, we calculate the annihilation rate needed to match the thermal relic cross section. The dominant annihilation process goes through an s -channel a exchange (Fig. 4)[37]. Note that even if kinematically allowed, the secluded t -channel decay of $\chi\bar{\chi} \rightarrow aa$ is p -wave suppressed [32, 95, 96]. In the non-relativistic limit the s -channel annihilation gives the following cross section [37]:⁴

$$\langle\sigma v\rangle = \frac{g_\chi^2 \sin^2 2\theta \tan^2 \beta}{8\pi} \frac{m_\chi^2}{m_a^4} \left[\left(1 - \frac{4m_\chi^2}{m_a^2} \right)^2 + \frac{\Gamma_a^2}{m_a^2} \right]^{-1} \sum_f N_C^f \frac{m_f^2}{v_{\text{SM}}^2} \sqrt{1 - \frac{m_f^2}{m_\chi^2}}, \quad (3.18)$$

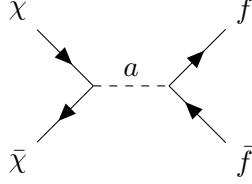


Figure 4. The s -channel a exchange annihilation of the DM fermion χ in 2HDM+ a model.

where the decay width of a is

$$\Gamma_a = \frac{g_\chi^2 \cos^2 \theta m_a}{8\pi} \sqrt{1 - \frac{4m_\chi^2}{m_a^2}} + \sum_f \frac{N_C^f m_f^2 \xi_f^2 \sin^2 \theta m_a}{8\pi v_{\text{SM}}^2} \sqrt{1 - \frac{4m_f^2}{m_a^2}}. \quad (3.19)$$

As discussed above, the thermal relic cross section for Dirac fermion dark matter is given by $\langle\sigma v\rangle \approx 4.4 \times 10^{-26}$ cm³/s (Eq. 3.4) in the relevant mass range. The original paper on this model (Ref. [37]) quoted a band of $\langle\sigma v\rangle = 1 - 5 \times 10^{-26}$ cm³/s, but based on a cross-comparison we believe that this is the equivalent cross section if the DM candidate were a Majorana fermion (i.e. divided by a factor of 2). We thus show the region with the cross section for Dirac fermion DM:

$$\langle\sigma v\rangle \sim (2 - 10) \times 10^{-26} \text{ cm}^3\text{s}^{-1}. \quad (3.20)$$

We have checked that this band is equivalent to the band shown in Ref. [37].

3.2.2 Direct detection

An advantage of the pseudoscalar model is that it can evade direct detection at tree level. The tree level interaction is spin-dependent [97] and suppressed by momentum transfer [98, 99]. A spin-independent interaction is generated at one-loop level (Fig. 5).

⁴Note this expression corrects a typo in the phase space factor from Ref. [37].

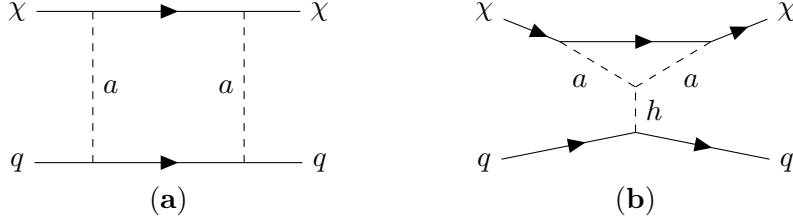


Figure 5. The representative one-loop diagrams for direct detection for the 2HDM+ a model, describing the scattering of the DM particle χ with quarks q . (a) describes the box diagram with exchange of the pseudoscalar a ; (b) is the triangle diagram involving Higgs exchange.

We can write down the one-loop effective interaction between χ and q from Fig. 5(a) [37]:

$$\mathcal{L}_{(a)} = \sum_{\text{down type } q} \frac{m_q^2 g_\chi^2 \tan^2 \beta \sin^2 2\theta}{128\pi^2 m_a^2 (m_\chi^2 - m_q^2)} \left(F\left(\frac{m_\chi^2}{m_a^2}\right) - F\left(\frac{m_q^2}{m_a^2}\right) \right) \frac{m_\chi m_q}{v_{\text{SM}}^2} \chi \bar{\chi} q \bar{q}, \quad (3.21)$$

with the corresponding loop integral

$$F(x) = \frac{2}{3x} (4 + f_+(x) + f_-(x)), \quad (3.22)$$

and

$$f_\pm(x) = \frac{1}{x} \left(1 \pm \frac{3}{\sqrt{1-4x}} \right) \left(\frac{1 \pm \sqrt{1-4x}}{2} \right)^3 \log \left(\frac{1 \pm \sqrt{1-4x}}{2} \right), \quad (3.23)$$

and from Fig. 5(b) [37]:

$$\mathcal{L}_{(b)} = \frac{(m_A^2 - m_a^2) \sin^2 2\theta g_\chi^2}{64\pi^2 m_h^2 m_a^2} G\left(\frac{m_\chi^2}{m_a^2}, 0\right) \frac{m_\chi m_q}{v_{\text{SM}}^2} \chi \bar{\chi} q \bar{q}, \quad (3.24)$$

with the corresponding loop integral

$$G(x, y) = -4i \int_0^1 dz \frac{z}{\mathcal{F}^{1/2}(x, y, z)} \times \ln \left(\frac{\mathcal{F}^{1/2}(x, y, z) + iy(1-z)}{\mathcal{F}^{1/2}(x, y, z) - iy(1-z)} \right), \quad (3.25)$$

and

$$\mathcal{F}(x, y, z) = y (4(1-z) + 4xz^2 - y(1-z)^2). \quad (3.26)$$

Note that $G(0, 0) = 1$.

For $\tan \beta \lesssim 100$, Fig. 5(b) dominates over Fig. 5(a) [79]. We can then simplify the expression, taking $\langle N | \sum_q m_q q \bar{q} | N \rangle \approx 330 \text{ MeV}$ [100]:

$$\begin{aligned} \sigma_{\text{SI}} &= \frac{\mu_{\chi N}^2}{\pi} \left[\frac{(m_A^2 - m_a^2) \sin^2 2\theta g_\chi^2}{64\pi^2 m_h^2 m_a^2} G\left(\frac{m_\chi^2}{m_a^2}, 0\right) \frac{m_\chi}{v_{\text{SM}}^2} \langle N | \sum_q m_q q \bar{q} | N \rangle \right]^2 \\ &\approx 2.2 \times 10^{-49} \text{ cm}^2 \left(\frac{m_A}{800 \text{ GeV}} \right)^4 \left(\frac{m_a}{50 \text{ GeV}} \right)^{-4} \left(\frac{m_\chi}{30 \text{ GeV}} \right)^2 \left(\frac{\theta}{0.1} \right)^4 \left(\frac{g_\chi}{0.5} \right)^4 \left(\frac{\langle N | \sum_q m_q q \bar{q} | N \rangle}{330 \text{ MeV}} \right)^2. \end{aligned} \quad (3.27)$$

We will compare this prediction to the latest LUX-ZEPLIN result [43].

3.2.3 Gamma-ray line search

The gamma-ray line search from the Fermi Gamma-Ray Space Telescope experiment [44] offers a tight constraint on the one-loop process $\chi\bar{\chi} \rightarrow \gamma\gamma$ (Fig. 6) which produces mono-energetic gamma-ray photons.

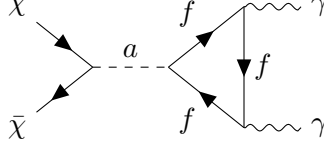


Figure 6. The representative Feynman diagram for one-loop $\chi\bar{\chi} \rightarrow \gamma\gamma$ process with a loop involving SM fermions f . This process gives a monochromatic gamma-ray line that can be constrained with data from the Fermi Gamma-Ray Space Telescope.

We consider the effective Lagrangian [101]:

$$\mathcal{L} \supset iy_\chi a \bar{\chi} \gamma^5 \chi + \sum_f iy_f a \bar{f} \gamma^5 f. \quad (3.28)$$

This effective Lagrangian is related to the type II 2HDM+ a model by

$$y_f = \begin{cases} \frac{m_f}{v_{\text{SM}}} \frac{\sin \theta}{\tan \beta} & \text{up-type quarks} \\ \frac{m_f}{v_{\text{SM}}} \sin \theta \tan \beta & \text{down-type quarks and leptons} \end{cases}, \quad (3.29)$$

$$y_\chi = g_\chi \cos \theta. \quad (3.30)$$

We can write down the one-loop level cross section:

$$\langle \sigma_{\chi\bar{\chi} \rightarrow \gamma\gamma} \rangle = \frac{y_\chi^2 \alpha^2}{4\pi^3} \frac{|\sum_f N_C^f Q_f^2 y_f m_f \mathcal{F}(m_\chi^2/m_a^2)|^2}{(4m_\chi^2 - m_a^2)^2 + m_a^2 \Gamma_a^2}, \quad (3.31)$$

where Q_f is the electric charge of fermion f , and

$$\mathcal{F} = \begin{cases} \arcsin^2(\sqrt{x}) & \text{if } x \leq 1 \\ -\frac{1}{4} \left[\log \left(\frac{1+\sqrt{1-1/x}}{1-\sqrt{1-1/x}} \right) - i\pi \right]^2 & \text{if } x > 1 \end{cases}. \quad (3.32)$$

We will compare this to the Fermi gamma-ray line search constraint from Ref. [44].

3.2.4 B-physics

The branching ratio of the rare decay $B_s^0 \rightarrow \mu^+ \mu^-$ constrains the parameters of the 2HDM+ a model [37, 102].

The relationship between the 2HDM branching ratio and the SM branching ratio for $B_s^0 \rightarrow \mu^+ \mu^-$ is [37, 103–105]:⁵

$$\text{Br}(B_s^0 \rightarrow \mu^+ \mu^-) \simeq \text{Br}(B_s^0 \rightarrow \mu^+ \mu^-)_{\text{SM}} \times \left| 1 + \frac{m_b m_{B_s} \tan^2 \beta \sin^2 \theta}{m_{B_s}^2 - m_a^2} \frac{f(x_t, y_t, r)}{Y(x_t)} \right|^2, \quad (3.33)$$

⁵Ref. [37] quotes this expression for $m_a \ll m_Z$, but we believe that the expression is valid for $m_a \ll m_A$.

where $x_t = m_t^2/m_W^2$, $y_t = m_t^2/m_{H^\pm}^2$, $r = m_{H^\pm}^2/m_W^2$,

$$f(x, y, r) = \frac{x}{8} \left[-\frac{r(x-1)-x}{(r-1)(x-1)} \log r + \frac{x \log x}{(x-1)} - \frac{y \log y}{(y-1)} + \frac{x \log y}{(r-x)(x-1)} \right], \quad (3.34)$$

and $Y(x)$ the Inami-Lim function:

$$Y(x) = \frac{x}{8} \left[\frac{x-4}{x-1} \log x + \frac{3x \log x}{(x-1)^2} \right]. \quad (3.35)$$

We will compare this to the SM prediction of $(3.66 \pm 0.14) \times 10^{-9}$ and the measured value of $3.09^{+0.46+0.15}_{-0.43-0.11} \times 10^{-9}$ [106]. We take the one-sided 95% exclusion limit as the upper bound of the branching ratio.

Note that other flavor anomalies might constrain the class of 2HDM models as well. Variants of the 2HDM model, such as a type-II 2HDM model with an extended Yukawa structure [107], have been explored to explain several persistent flavor anomalies, including potential deviations from the SM predictions observed in $b \rightarrow c\tau^-\nu$ and $b \rightarrow sl^+l^-$ transitions [102, 108]. Other loop-induced processes like $b \rightarrow s\gamma$ require a relatively heavy charged Higgs (typically $M_{H^\pm} \gtrsim 600\text{GeV}$ in Type II scenarios) [109]. The mass of the charged Higgs is not the main focus of this paper; we require the charged Higgs to be heavy enough to evade the other constraints while preserving the perturbativity of the 2HDM+ a model.

3.2.5 Invisible Higgs decay

In the 2HDM+ a model, it is possible for the SM-like Higgs h to decay into dark sector particles, thereby creating an invisible Higgs decay. The invisible Higgs decay is constrained by the LHC [110]. In this section, we consider the effective Lagrangian

$$\mathcal{L} \supset \lambda h a a + i y_\chi a \bar{\chi} \gamma^5 \chi, \quad (3.36)$$

where

$$\lambda = \frac{(m_A^2 - m_a^2) \sin^2 2\theta}{2v_{\text{SM}}}, \quad y_\chi = g_\chi \cos \theta. \quad (3.37)$$

The usual tree-level two-body decay $h \rightarrow aa$ (Fig. 7(a)) only meaningfully constrains the part of the parameter space where $m_a < \frac{1}{2}m_h$. Therefore, to calculate the constraints at higher m_a , where kinematically it might still be possible for the SM-like Higgs h to decay into the lighter χ through an off-shell a , we also consider the following decay channels:

- the one-loop decay $h \rightarrow aa\chi$ (loop) $\rightarrow \chi\bar{\chi}$ for $m_\chi < \frac{1}{2}m_h$ (Fig. 7(b)),
- the three-body decay $h \rightarrow a^*a \rightarrow a\chi\bar{\chi}$ for $m_a + 2m_\chi < m_h$ (Fig. 7(c)),
- the four-body decay $h \rightarrow a^*a^* \rightarrow \chi\bar{\chi}\chi\bar{\chi}$ for $m_\chi < \frac{1}{4}m_h$ (Fig. 7(d)).

The one-loop decay The one-loop contribution to the decay width of $h \rightarrow \chi\bar{\chi}$ is [37]:

$$\Gamma_{\text{loop}} = \left(\frac{\lambda g_\chi^2}{32\pi^2 m_a^2} \right)^2 \frac{m_h}{8\pi} G \left(\frac{m_\chi^2}{m_a^2}, \frac{q^2}{m_a^2} \right)^2 \left(1 - \frac{4m_\chi^2}{m_h^2} \right)^{\frac{3}{2}}, \quad (3.38)$$

where G is the same loop integral as (3.25).

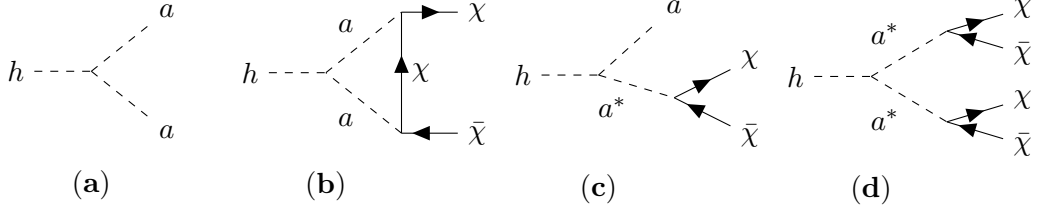


Figure 7. The representative Feynman diagrams for (a) $h \rightarrow aa$, (b) $h \rightarrow aa\chi$ (loop) $\rightarrow \chi\bar{\chi}$, (c) $h \rightarrow aa^* \rightarrow a\chi\bar{\chi}$, and (d) $h \rightarrow a^*a^* \rightarrow \chi\bar{\chi}\chi\bar{\chi}$.

Three and four-body decay For the three-body decay, we parameterize the initial state h and the final-state a, χ and $\bar{\chi}$ to have momenta p, p_1, p_2, p_3 respectively. We then obtain the spin-averaged squared matrix element as:

$$\frac{1}{4} \sum_{\text{spins}} |\mathcal{M}|^2 = \frac{\lambda^2 y_\chi^2}{|(p - p_1)^2 - m_a^2 + i\Gamma_a|^2} (p_2 \cdot p_3 - m_\chi^2). \quad (3.39)$$

We similarly calculate the four-body decay $h \rightarrow a^*a^* \rightarrow \chi\bar{\chi}\chi\bar{\chi}$ by parameterizing the momenta of the initial-state h and final state $\chi\bar{\chi}\chi\bar{\chi}$ to be p, p_1, p_2, p_3, p_4 respectively. We find:

$$\frac{1}{16} \sum_{\text{spins}} |\mathcal{M}|^2 = \frac{\lambda^2 y_\chi^4}{|(p_1 + p_2)^2 - m_a^2| (p - p_1 - p_2)^2 - m_a^2 + i\Gamma_a|^2} (p_1 \cdot p_2 - m_\chi^2) (p_3 \cdot p_4 - m_\chi^2). \quad (3.40)$$

We use a Monte Carlo simulation to calculate the phase space factor with HAZMA [111]:

$$d\Gamma = \frac{(2\pi)^4}{2m_h} |\mathcal{M}|^2 d\Phi. \quad (3.41)$$

We then compare the decay width of the invisible decay to the upper bound of 0.105 on the invisible branching ratio of the Higgs boson from ATLAS [110] at 95% confidence level and the Higgs boson’s decay width of 4.1 MeV [84].

3.2.6 Collider searches

In the LHC, the pseudoscalar mediator a can be produced (on-shell or off-shell), and then decay into the dark fermion χ . In the visible sector, this process looks like the production of a single SM particle, dubbed the “mono- X ” search. The leading collider searches, according to ATLAS [81], are the mono-Higgs and the mono- Z search in Fig. 8.

We explored both the mono-Higgs and mono- Z searches with MADGRAPH [112] and found that for the parameter space under consideration, the mono- Z search has a larger reach than the mono-Higgs search. We thus focus on the mono- Z search.

For the modeling of the mono- Z search, we use MADGRAPH 5 version 2.9.21 [112] to generate the hard scattering events at leading order for the $b\bar{b}$ mode of production of the DM at high $\tan\beta$, using the 2HDM Universal FeynRules Output (UFO) from Ref. [80]. We use NNPDF23_LO_AS.0130_QED [113] in LHAPDF 6 [114] for the parton distribution

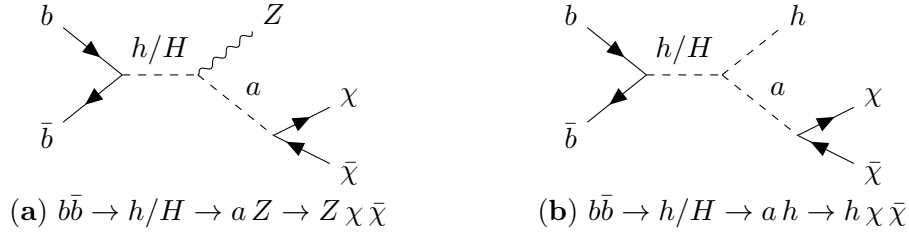


Figure 8. The representative mono- Z and mono-Higgs Feynman diagrams for the $b\bar{b}$ initial state in high $\tan\beta$ regime. The neutral Higgs h or H decays to a pseudoscalar a plus a visible Z or h , and then a decays invisibly to $\chi\bar{\chi}$.

function (PDF). We then use PYTHIA 8.311 [115] for parton showering and hadronization, and DELPHES 3.5.0 [116] with FASTJET 3.4.3 [117] for detector simulation.

The cuts we employ to process the simulation data are as follows, matching the analysis of Ref. [118]:

- Exactly two oppositely charged electrons or muons, with:
 - Leading lepton $p_T > 30$ GeV,
 - Subleading lepton $p_T > 20$ GeV,
 - Dilepton invariant mass $76 < m_{\ell\ell} < 106$ GeV.
- Missing transverse momentum $E_T^{\text{miss}} > 90$ GeV, missing- E_T significance $S_{E_T^{\text{miss}}} > 9$;
- Leptons must be relatively close in angle: $\Delta R(\ell, \ell) < 1.8$;
- Events containing one or more tagged b -jets are rejected (to reduce top-quark backgrounds).

We then compare our result to the 3σ upper limit in Ref. [118].

4 Results

Having laid out how to calculate the constraints on the secluded hypercharge model and the 2HDM+ a model, we will now scan the parameter space to obtain the updated exclusion plots. In particular, we use the following updated constraints:

- Direct detection: the latest result from the LZ experiment in 2024 [43];
- CMB bound: the latest Planck result in 2018 [87];
- Accelerator and beam dump search for dark photon: the summary plot in [92];
- Gamma-ray line search: a recent analysis using data from the Fermi Gamma-Ray Space Telescope result in 2023 [44];
- Collider measurements: the measurements from LHC run 2 of the invisible Higgs decay [119], the $B_s^0 \rightarrow \mu^+\mu^-$ decay [106], the mono-Higgs search [120], and the mono- Z search [81, 118] for the 2HDM+ a model.

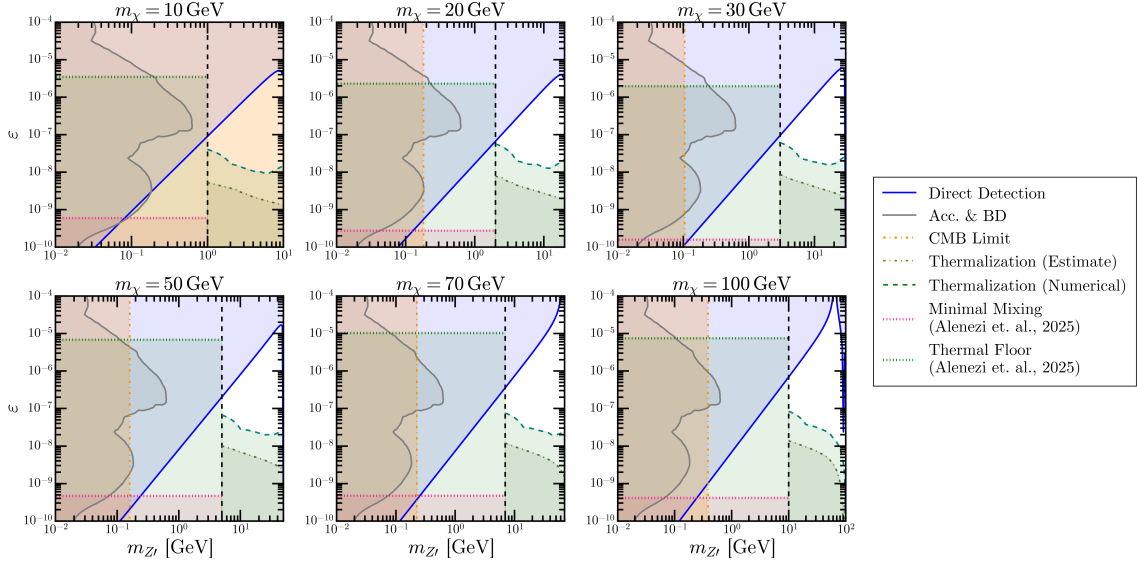


Figure 9. Constraints for the secluded hypercharge model at different m_χ . Note that for each m_χ , we plotted the corresponding $m_{Z'}$ from 1×10^{-2} GeV up to m_χ . The black dotted lines indicate where $m_{Z'} = 0.1 m_\chi$. At $m_{Z'} \sim 0.1 m_\chi$, our result is similar to the thermalization floor in Ref. [64], which also did not include in medium effect (insignificant at $m_{Z'} \gtrsim T$). We also show the limit from Refs. [65] for comparison. In general, there is still parameter space open at higher $m_{Z'}$.

4.1 The secluded hypercharge model

After scanning the parameter space of the secluded hypercharge model, we obtain the exclusion plot for the secluded hypercharge model in Fig. 9.

We see that large parts of the phase space are excluded, but there is still some available phase space at higher $m_{Z'}$. The accelerator and beam dump search is always sub-dominant to the direct detection search in our parameter space (although relatively modest changes to the scenario, such as making χ a pseudo-Dirac fermion with a modest mass splitting between its components, may alter this conclusion). Assuming the standard cosmological history and the thermal relic annihilation cross section, the CMB bound excludes all parameter space where $m_\chi \lesssim 10$ GeV while posing a modest constraint for low $m_{Z'}$ at larger m_χ due to the Sommerfeld enhancement at low $m_{Z'}/m_\chi$. In general, our constraints disfavor a large hierarchy between $m_{Z'}$ and m_χ .

The thermalization bound, together with direct detection, constrains the viable range of ϵ for higher $m_{Z'}$, beyond the current reach of accelerators. For lighter $m_{Z'} < 0.1 m_\chi$, the results of Ref. [65] imply that the DM must always be in the “leak-in” or “reannihilation” regimes, rather than undergoing standard thermal freezeout. This implies that α_D , and consequently the present-day DM annihilation cross-section, is *suppressed* relative to the standard thermal relic value. The degree of suppression found in Ref. [65] is typically up to a factor of few in α_D (corresponding to up to ~ 1 order of magnitude in the cross section); this region may thus have difficulty matching higher estimates of the cross section needed to explain the GCE, although it could potentially alleviate the tension with bounds from

dwarf galaxies.

For larger $m_{Z'} > 0.1m_\chi$, we have provided both an estimate of the thermalization floor based on the Z' decay lifetime, and the results of solving the full Boltzmann equations. The refined thermalization threshold for ε from the latter calculation, as a function of m_χ and $m_{Z'}$, is slightly higher than our estimate based on the Z' decay rate, but in qualitatively good agreement, and confirms that for $m_{Z'}$ within an order of magnitude of m_χ , there can be open parameter space for several orders of magnitude in ε . As in the case with $m_{Z'} < 0.1m_\chi$, the thermalization floor is also not a hard exclusion; points below this floor may still accommodate the GCE, but will correspond to a lower present-day annihilation cross section.

Our results show that the CMB constraint is powerful for $m_\chi \lesssim 10$ GeV, but at higher masses rapidly becomes irrelevant (unless the Z' mass is small enough to allow for large Sommerfeld enhancement, but for this model this region is excluded by direct detection).

At high $m_{Z'}$, there is still a window of parameter space that evades direct detection limits while still having a large enough mixing to ensure full equilibration between DM and SM in the early universe. We offer a discussion of the approximate dependence of different constraints in Table 1.

Allowing an annihilation cross section modestly lower than the canonical thermal relic cross section—which might still produce the correct thermal relic density, due to a modified cosmological history or the presence of additional annihilation channels—weakens the CMB constraint and marginally relaxes the direct detection limit. Nevertheless, the allowed parameter region remains essentially unchanged.

Note that when $m_{Z'} \lesssim 300$ MeV, the annihilation might in any case have difficulty matching the GCE spectra (here the appropriate degrees of freedom are pions instead of quarks, due to the QCD phase transition [121]). However, from Fig. 9, the allowed phase space already requires $m_{Z'} > 300$ MeV due to the direct detection constraint, so we do not consider this regime in detail, but we show the full parameter space for completeness.

Table 1. The approximate dependence of different constraints for the secluded hypercharge model, assuming $m_{Z'} \ll m_\chi$.

Process	ε	$m_{Z'}$	m_χ	g_D
$\langle\sigma v\rangle$	\times	\times	$1/m_\chi^2$	g_D^4
CMB	\times	\times	$1/m_\chi^3$	g_D^4
Direct Detection	ε^2	$1/m_{Z'}^4$	\times	g_D^2
Standard Cosmology	ε^2	$m_{Z'}$	\times	\times

4.2 The 2HDM+ a model

For the 2HDM+ a model, we first compare our updated result to the exclusion plot from Ref. [37] in Fig. 10, for the benchmark parameter point they chose in that work of $g_\chi = 0.5$, $m_\chi = 30$ GeV, and $\tan\beta = 40$.

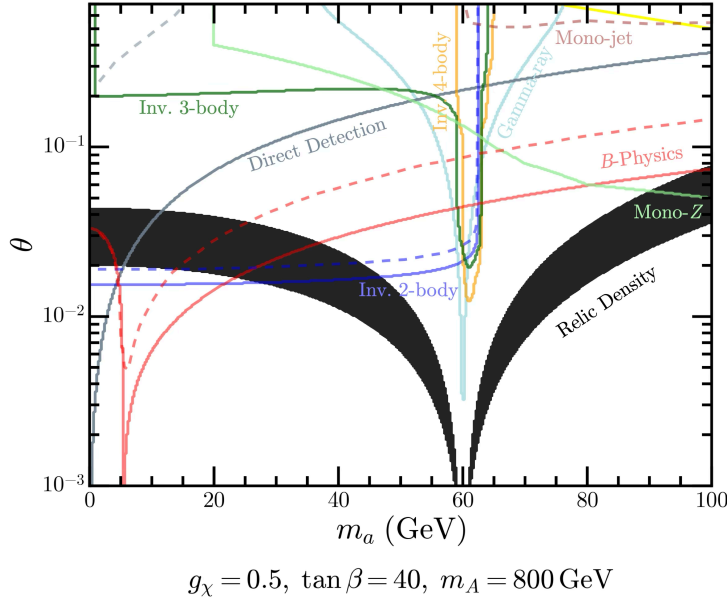


Figure 10. Comparison between the updated constraints and the constraints from [37] in 2014. The dashed lines indicate old constraints while the solid lines indicate updated constraints. The black regions indicate parameters that reproduce the thermal relic density. The yellow line on the top-right of the plot is the mono-Higgs search constraint, which is much weaker than the mono- Z search constraint in our parameter space. The parameters we hold constant for this plot are: $g_\chi = 0.5$, $m_\chi = 30 \text{ GeV}$, and $\tan\beta = 40$.

Compared to the old constraints from Ref. [37], the direct detection bound improves significantly, but it is still generally subleading compared to the B -physics bound which is improved with data from the LHC Run 2. The B -physics bound excludes regions with high θ and low m_a , although heavier m_a regions will likely have improved coverage with the data sets collected at the high-luminosity LHC (HL-LHC). There is a marginal improvement for the invisible Higgs decay including 3-body and 4-body decay, which excludes regions of moderate-to-high θ at $m_a < \frac{1}{2}m_h$. Collider searches exclude regions of very high θ and high m_a . The Mono- Z collider search from LHC Run 2 gives a more stringent bound compared to the mono-jet collider bound in [37]. Further, new constraints are considered: the gamma-ray line search constraint eliminates open parameter space for lower $\tan\beta$, effectively because the signal is enhanced by the higher coupling to top quarks at lower $\tan\beta$. However, there is still a substantial amount of open parameter space.

We then scan through the parameter space and obtain the results for different values of g_χ , $\tan\beta$, and m_χ in Fig. 11 and 12.

We can see that at relatively lower $\tan\beta$, the gamma-ray line constraint is particularly strong (especially at lower m_χ). At large $\tan\beta$, the B -physics constraint is dominant for small θ and m_a . The invisible decay constraints largely eliminate $m_a < \frac{1}{2}m_h$ regions, while the collider constraints exclude parameter space at higher m_a , higher $\tan\beta$, and smaller m_χ . In general, the parameter space that survives is: high $\tan\beta \gtrsim 10$, high $m_\chi \gtrsim 10 \text{ GeV}$,

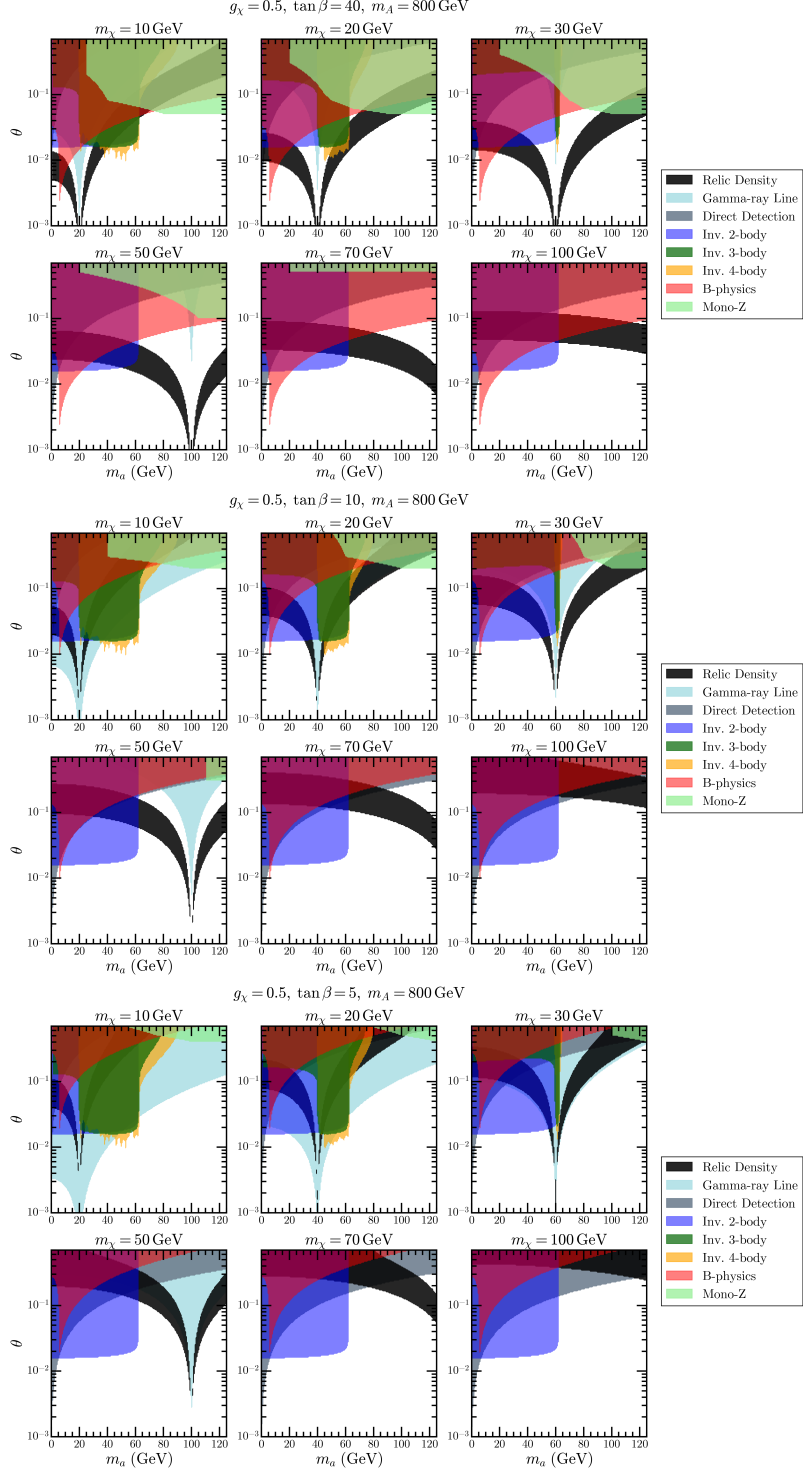


Figure 11. Constraints for the 2HDM+a model at $g_\chi = 0.5$. The mono-Z search constraints are only shown for $m_a \geq 20 \text{ GeV}$ as complications might arise at very low mediator mass; additionally, the mono-Z search constraints are not leading for $m_a \leq 20 \text{ GeV}$. The 3-body and 4-body invisible decay have numerical instabilities at $m_a \leq 1/2 m_h$. In general, the available parameter space is: high $\tan\beta \gtrsim 10$, high $m_\chi \gtrsim 10 \text{ GeV}$, low $\theta \lesssim 0.1$, and moderate-to-high $m_a \sim \mathcal{O}(2m_\chi)$ but not necessarily very close to resonance.

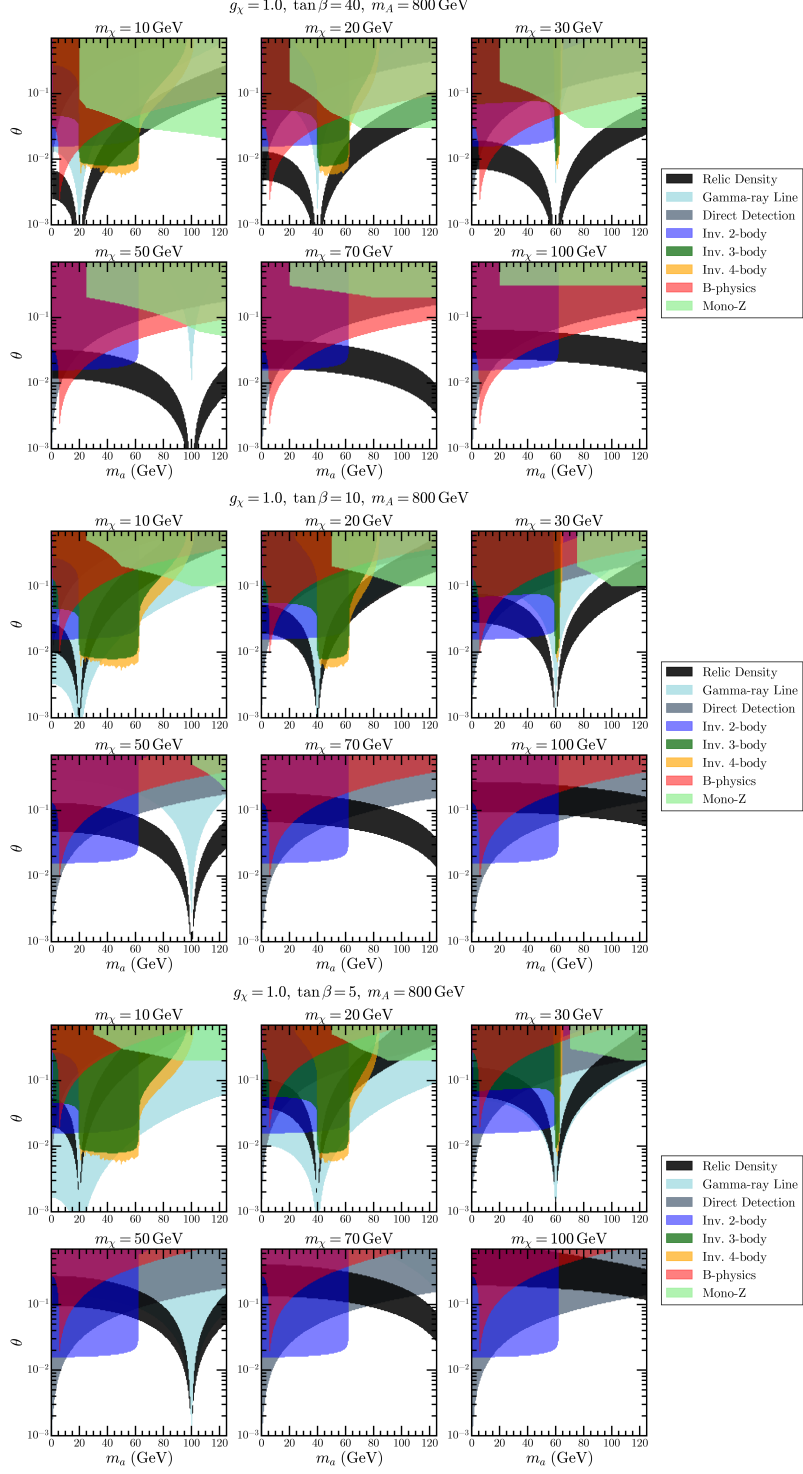


Figure 12. Constraints for the 2HDM+a model at $g_\chi = 1$, with the same plotting considerations and similar available parameter space as Fig. 11.

low $\theta \lesssim 0.1$, and moderate-to-high $m_a \sim \mathcal{O}(2m_\chi)$ (not necessarily very close to resonance). Note that in general, at higher $\tan\beta$, lower m_χ is allowed.

We therefore need a very large splitting in the vevs of the two Higgs bosons and for the pseudoscalar mediator to couple to down-type quarks and leptons much better than up-type quarks. A higher DM candidate mass is also preferred, which might push the available phase space away from the masses suitable for the GCE spectrum. Lower mixing between a and A is also favored which decouples the dark sector from the Higgs sector.

We also offer a discussion of the approximate dependence of different constraints at high $\tan\beta$ in Table 2.

Table 2. The approximate dependence of different constraints of the 2HDM+ a model at small θ , high $\tan\beta$, and $m_\chi \ll m_a \ll m_A = m_{H^\pm}$. Note that the B physics constraint also is dependent on m_{H^\pm} .

Process	θ	$\tan\beta$	m_a	m_χ	g_χ	m_A
$\langle\sigma v\rangle$	θ^2	$\tan^4\beta$	$1/m_a^4$	m_χ^2	g_χ^2	\times
Direct Detection	θ^4	\times	\times	m_χ^2	g_χ^4	m_A^4
Gamma-ray Line	θ^2	$\tan^2\beta$	$1/m_a^8$	m_χ^4	g_χ^2	\times
$B_s^0 \rightarrow \mu^+\mu^-$	θ^4	$\tan^4\beta$	$1/m_a^4$	\times	\times	\times
$h \rightarrow aa$ onshell	θ^4	\times	\times (if $m_a \ll \frac{1}{2}m_h$)	\times	\times	m_A^4
Invisible One-Loop Decay	θ^4	\times	$1/m_a^4$	\times	g_χ^4	m_A^4
Invisible 3-Body Decay	θ^4	\times	$1/m_a^2$	\times	g_χ^2	m_A^4
Invisible 4-Body Decay	θ^4	\times	$1/m_a^4$	\times	g_χ^4	m_A^4
Mono- Z	θ^2	$\tan^2\beta$	$1/m_a^2$	\times	g_χ^2	\times

Close to resonance (i.e. $m_a \approx 2m_\chi$), a smaller mixing θ is required to obtain the thermal relic cross section and so this region is generically less constrained. However, sufficiently close to the resonance the s -wave cross section may be enhanced at low velocities relative to freezeout, potentially overproducing the GCE. Roughly speaking, near the Breit-Wigner resonance the denominator of the (squared) propagator has the form $(2m_\chi + m_\chi v^2)^2 - m_a^2 \approx (2m_\chi)^2 - m_a^2 + 4m_\chi^2 v^2$ (where v is the velocity of one of the DM particles in the center-of-momentum frame), so the velocity-dependent term is important for $v^2 \gtrsim |1 - (m_a/(2m_\chi))^2|$. The characteristic velocity at freeze-out corresponds to $v^2 \sim 0.1$, so we can expect there to be non-trivial velocity evolution between freeze-out and the present day for $m_a/(2m_\chi) \sim 0.95 - 1.05$. Since there is substantial unconstrained parameter space available without relying on close proximity to the resonance, we do not explore this region further in this work.

5 Future Projections

Finally, we will project the prospects for improvements on these constraints—or for a discovery—as the experimental sensitivity continues to advance in the coming years.

- We will consider the neutrino floor as the direct detection forecast [122]. This can be achieved in the next-generation experiments such as DARWIN [123] or XLZD [124].
- For the beam dump and accelerator search for the secluded hypercharge model, we include the latest projection for SHiP experiment [125], which has the highest sensitivity to the parameter space we are searching for [65].
- For the LHC mono- Z search, we roughly estimate that the LHC increases the luminosity by one order of magnitude with the HL-LHC [126]; we then scale the current collider bounds to match this estimate.
- For the B -physics search, the HL-LHC is expected to improve the uncertainty of the branching ratio $\text{Br}(B_s^0 \rightarrow \mu^+ \mu^-)$ to around 10% [127]. The resulting upper bound is not improved compared to the current constraint.
- For the invisible Higgs decay branching ratio, the HL-LHC will give a constraint of 2.5% at 95% confidence [128].
- For the gamma-ray line search, we compare the Fermi telescope bound to the sensitivity forecast of the upcoming Cherenkov Telescope Array (CTA) [129] and the proposed Advanced Particle-astrophysics Telescope (APT) [130, 131]. We find that at the DM candidate mass range of ~ 50 GeV range that we are interested for the GCE, the bound of the CTA is not improved compared to our current Fermi telescope limit, while the proposed APT improves the constraint by more than an order of magnitude [131, 132]. We optimistically improve the cross section sensitivity by an order of magnitude and use it in our forecast.

We therefore forecast the constraints of the secluded hypercharge model and the 2HDM+ a model in Fig. 13, 14, and 15.

For the secluded hypercharge model, we can see that the SHiP search would still remain subdominant to the direct detection search. There would be a marginal improvement from the direct detection limit at the neutrino floor; however, there would still be some parameter space left open at higher $m_{Z'}$.

For the 2HDM+ a model, we can see that the direct detection limit at the neutrino floor would be competitive with the B physics bound, especially at lower $\tan \beta \lesssim 10$. Improved invisible decay constraints would cut off most of the phase space where $m_a < \frac{1}{2}m_h$, with some heavier- m_a space constrained due to the 4-body invisible decay. The improved gamma-ray line search would become more powerful at lower $\tan \beta \lesssim 10$ and lower $m_\chi \lesssim 50$ GeV (although note that a factor-of-ten improvement in sensitivity to gamma-rays could independently possibly exclude or confirm the GCE based on dwarf galaxy observations). Higher $\tan \beta$ allows lower $m_\chi \sim 30$ GeV. The higher luminosity mono- Z search would cut off the phase space at high $m_a \gtrsim 80$ GeV and $\theta \gtrsim 0.1$. However, even with all these improvements, we expect there would still be parameter space left untested at high $\tan \beta \sim 40$ and high $m_\chi \gtrsim 50$ GeV for a window around $m_a \sim \mathcal{O}(2m_\chi)$.

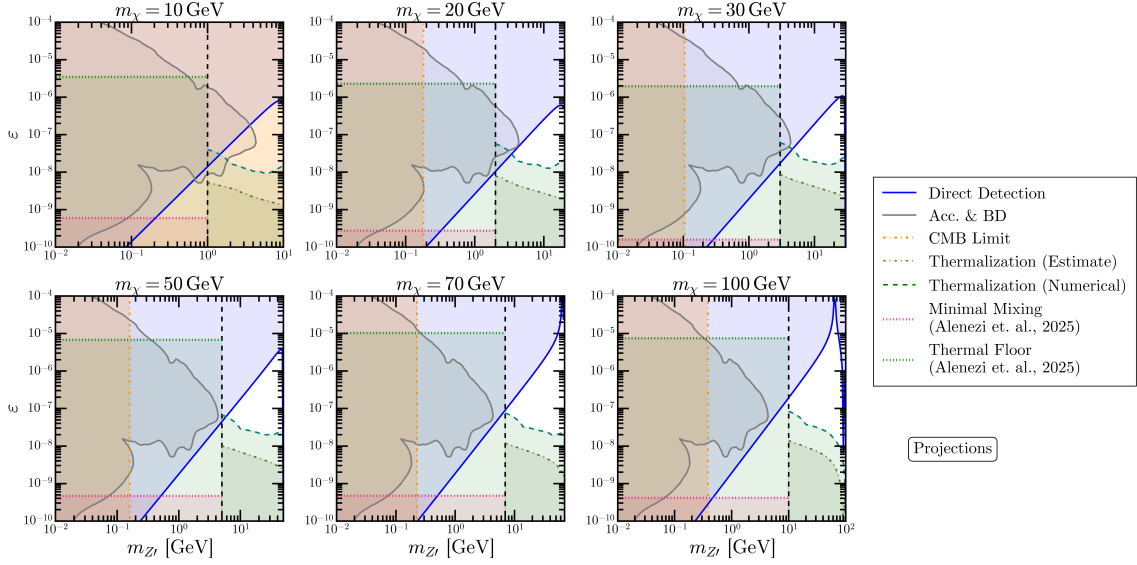


Figure 13. Forecast of constraints for the secluded hypercharge model at different m_χ . In general, there would still be some parameter space left open at higher $m_{Z'}$.

6 Conclusion

After updating the constraints for the secluded hypercharge model and the 2HDM+ a model, we see that there is still open parameter space that is broadly consistent with a thermal relic DM origin for the GCE. However, we note that the advent of experiments have eliminated a large part of this closing parameter space. Future experiments have the potential to further test new regions of parameter space, but will not fully exclude these scenarios in the absence of a detection (with the possible exception of improved gamma-ray sensitivity allowing model-independent tests of the GCE through observations of dwarf galaxies).

For the secluded hypercharge model, indirect bounds from the cosmic microwave background are constraining at the low end of the mass range ($m_\chi \lesssim 10$ GeV). At the opposite DM mass regime, while the CMB limits do place bounds on the Z' mass due to the presence of Sommerfeld enhancement, for thermal relics the constraints from direct detection (and to a lesser degree, accelerators) are always stronger (similar results are found in [133]). In general, these limits require the Z' mediator to be heavier than 1 – 2 GeV, in order to simultaneously maintain the assumption of a standard cosmological history. The limit on the mixing of the Z' with the SM hypercharge depends strongly on its mass, being constrained above by direct detection and below by the requirement of full equilibrium prior to freeze-out, but broadly speaking there is parameter space available when the DM mass is 10s of GeV, the Z' mass is in the range from a few GeV to the DM mass, and the mixing is in the range $\epsilon \sim 10^{-8} - 10^{-6}$.

For the 2HDM+ a model, it is harder to provide a simple summary as the parameter space is quite high-dimensional, but we can again make some general statements. There remains

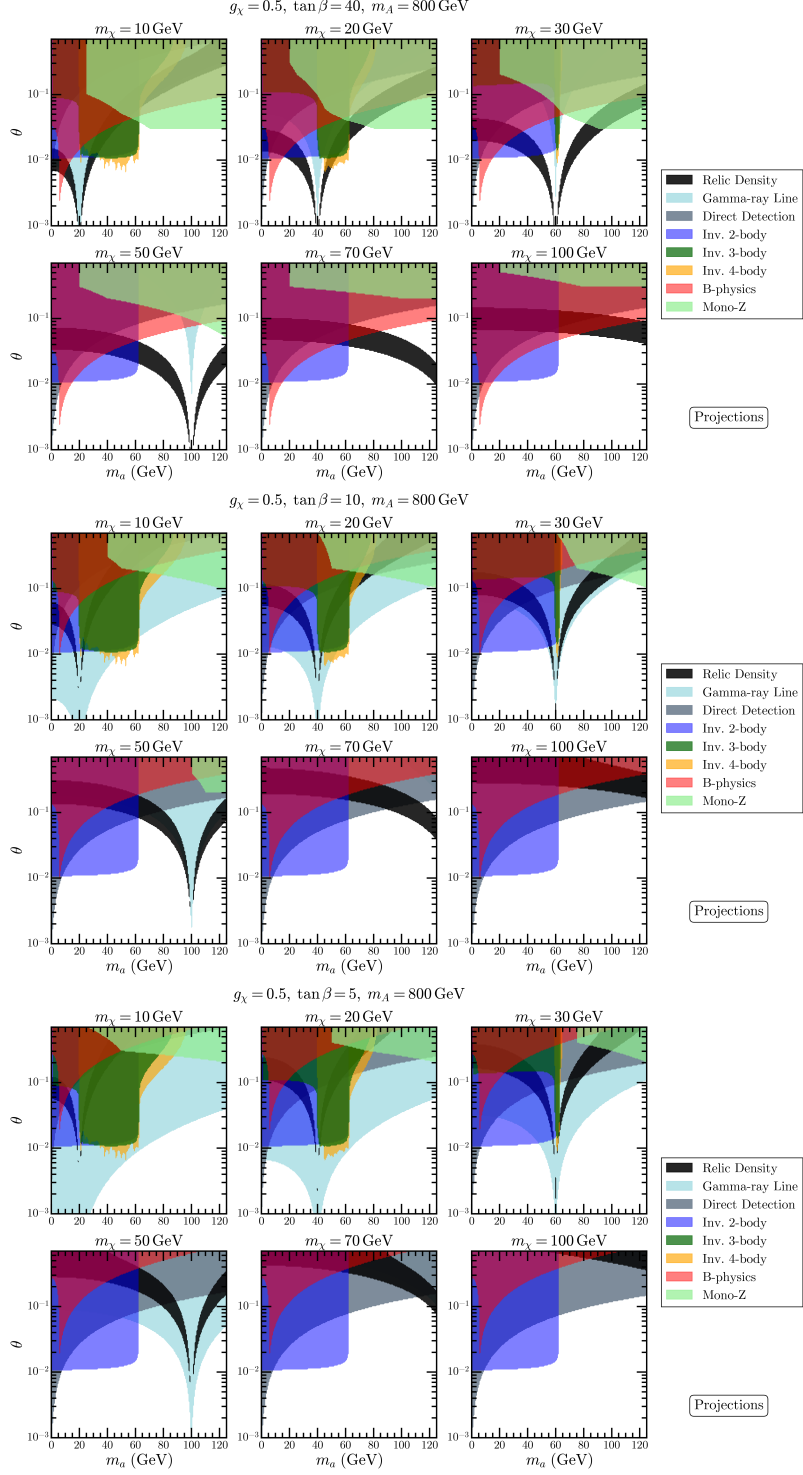


Figure 14. Forecast of constraints for the 2HDM+a model at $g_\chi = 0.5$. In general, there would still be parameter space available at $\tan\beta \sim 40$ and $m_\chi \gtrsim 50$ GeV for a window around $m_a \sim \mathcal{O}(2m_\chi)$.

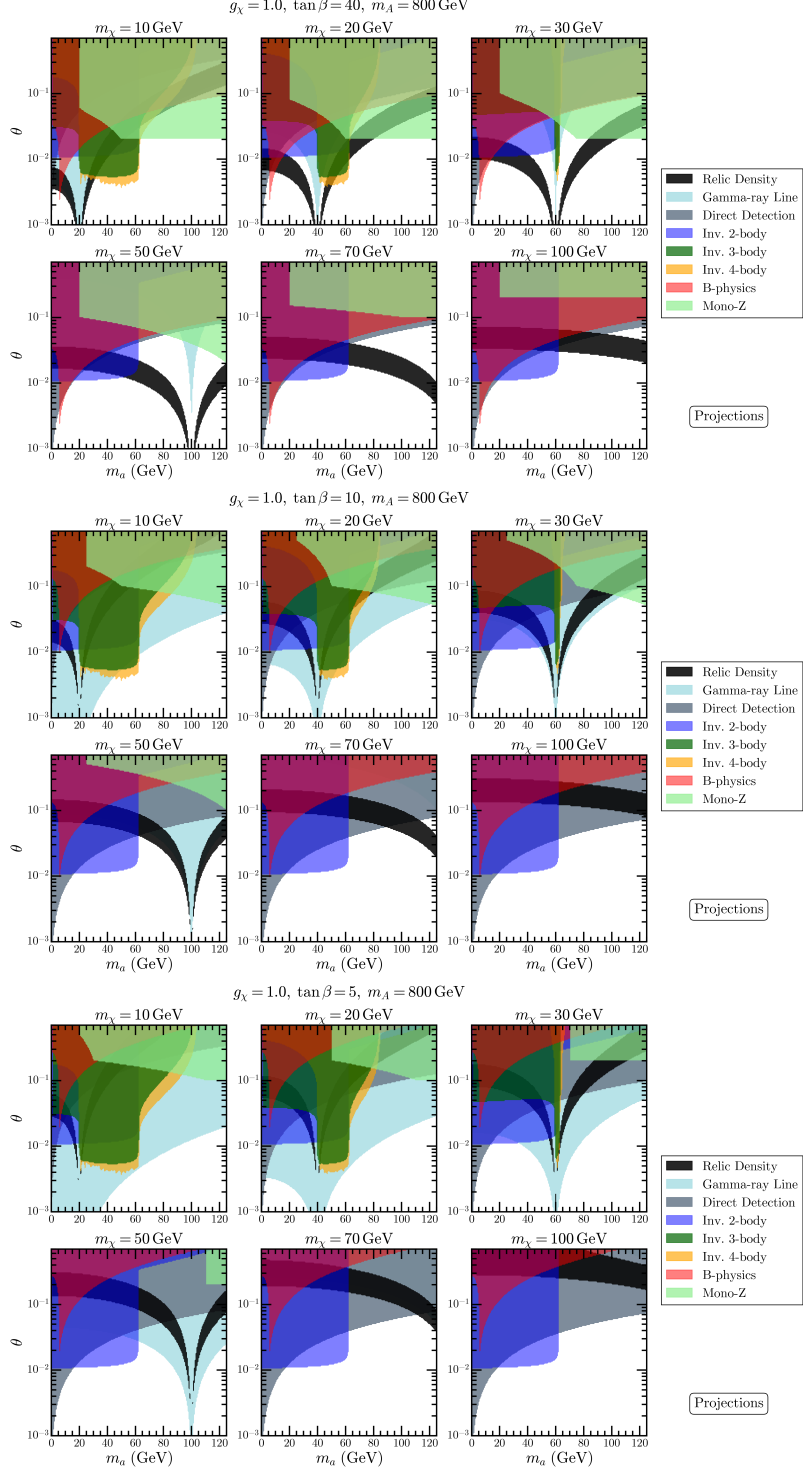


Figure 15. Forecast of constraints for the 2HDM+a model at $g_\chi = 1$, with similar available parameter space as Fig. 14.

open parameter space, with a preference for high $\tan\beta \gtrsim 10$, higher DM mass $m_\chi \gtrsim 30$ GeV, m_a for the light pseudoscalar mediator of the same order as $2m_\chi$ (but not requiring a fine-tuning to the resonance where $m_a = 2m_\chi$), and a small mixing angle $\theta \lesssim 0.1$ which controls the coupling of the a to the SM matter fields. At higher $\tan\beta$, the DM mass is less constrained and lower DM masses are permitted. In contrast to earlier studies, direct detection has now reached the sensitivity where it is beginning to test the parameter space where the model obtains the correct relic density, although it is often still less constraining than bounds from B physics.

A conclusion that we can draw from both of the benchmark models is that the union of cosmological and terrestrial experiments are necessary for the study of DM. While the fundamental origin of the GCE is not yet known, the next generation of experiments will provide important insight towards understanding the particle content and observable nature of DM in the universe. At the same time, we see in both of these examples that while terrestrial experiments have significantly narrowed the viable parameter space for a DM explanation of the GCE (and will continue to do so), there remains parameter space that will be very difficult to exclude with any set of null results at terrestrial experiments, emphasizing the importance of more model-independent tests of the GCE in dwarf galaxies and other astrophysical systems.

Acknowledgments

We would like to thank Gordan Krnjaic and Jessie Shelton for useful feedback and discussions. This work was supported by the U.S. Department of Energy (DOE) Office of High Energy Physics under Grant Contract No. DE-SC0012567. Y.H. was supported by the MIT Undergraduate Research Opportunities Program. T.R.S. and C.C. were supported in part by the Simons Foundation (Grant No. 929255). T.R.S. was supported during the course of this work by a Guggenheim Fellowship; the Edward, Frances, and Shirley B. Daniels Fellowship of the Harvard Radcliffe Institute; and the Bershadsky Distinguished Fellowship of the Harvard Physics Department.

A Calculation of the GCE spectra

With the parameters of the DM models, we can generate the corresponding GCE spectra. We obtain the photon fluxes dN_a/dE_γ at production per annihilation event from [134, 135], where E_γ is the energy of the photon. To convert the photon flux at production per annihilation event of Dirac fermions to the GCE signal $E_\gamma^2 dN_\gamma/dE$, we use [31, 136]

$$E_\gamma^2 \frac{dN_\gamma}{dE_\gamma} = E_\gamma^2 \frac{\langle\sigma v\rangle}{16\pi m_\chi^2} J(\Delta\Omega) \frac{dN_a}{dE_\gamma}. \quad (\text{A.1})$$

$J(\Delta\Omega)$ is the J -factor of the region of interest (ROI) $\Delta\Omega$ in the Galactic Center, which accounts for the distribution and the density of the DM halo in the Galactic Center.

The J -factor is calculated with [137]

$$J(\Delta\Omega) = \int_{\text{ROI}} d\Omega \int_0^\infty ds \rho^2(r(s, l, b)), \quad (\text{A.2})$$

where

$$r(s, l, b) = \sqrt{r_\odot^2 + s^2 - 2r_\odot s \cos l \cos b}, \quad (\text{A.3})$$

s is the distance along the line of sight (LOS), $r_\odot \simeq 8.5$ kpc is the distance between the sun and the Galactic Center, l and b are the galactic coordinates, and ρ is the density of the DM.

In the generalized Navarro-Frenk-White (gNFW) profile, the density of the DM can be written as [138]

$$\rho(r) = \rho_s \left(\frac{r}{r_s} \right)^{-\gamma} \left(1 + \frac{r}{r_s} \right)^{\gamma-3}, \quad (\text{A.4})$$

where γ is the inner slope, r_s is the scale radius, and ρ_s is the scale density. We take $r_s \simeq 20$ kpc, and the scale density ρ_s fixed by the local density $\rho(r_\odot) \approx 0.4 \text{ GeV cm}^{-3}$.

For the secluded hypercharge model, the dominant annihilation channel is $\chi\bar{\chi} \rightarrow Z'Z'$ followed by $Z' \rightarrow f\bar{f}$. We then calculate the kinematics of the cascade decay [31]: given the decay spectrum of $dN_a/dE_{\gamma,Z'}$ where $E_{\gamma,Z'}$ is the energy of photons in the rest frame of Z' , we can convert the spectrum to the energy of photons in the rest frame of χ , E_γ , by [31]:

$$\frac{dN_a}{dE_\gamma} = \frac{2m_{Z'}}{m_\chi} \int_{E_{\min}}^{E_{\max}} \frac{dE_{\gamma,Z'}}{E_{\gamma,Z'} \sqrt{1 - (2m_{Z'}/m_\chi)^2}} \frac{dN_a}{dE_{\gamma,Z'}}, \quad (\text{A.5})$$

where the integration limits

$$\begin{aligned} E_{\max} &= \min \left[\frac{m_{Z'}}{2}, \frac{E_\gamma m_\chi}{2m_{Z'}} \left(1 + \sqrt{1 - (2m_{Z'}/m_\chi)^2} \right) \right], \\ E_{\min} &= \frac{E_\gamma m_\chi}{2m_{Z'}} \left(1 - \sqrt{1 - (2m_{Z'}/m_\chi)^2} \right). \end{aligned} \quad (\text{A.6})$$

We then find the branching ratio from (3.5) and the annihilation spectra from Ref. [134, 135].

For the 2HDM+ a model, the available phase space favors s -channel annihilation of $\chi\chi \rightarrow b\bar{b}$. We then directly use the annihilation spectra from Ref. [134, 135].

We obtain the possible GCE spectra across different background models from Ref. [139], with an ROI of $|l| < 20^\circ, 2^\circ < |b| < 20^\circ$. We use a gNFW profile with $\gamma = 1.25$. The J -factor is then calculated to be

$$J(|l| < 20^\circ, 2^\circ < |b| < 20^\circ) \simeq 1.02 \times 10^{23} \text{ GeV}^2 \text{ cm}^{-5}. \quad (\text{A.7})$$

For the secluded hypercharge model, we select $m_\chi = 50$ GeV, $m_{Z'} = 15$ GeV, and $\langle\sigma v\rangle = 4.4 \times 10^{-26} \text{ cm}^3 \text{ s}^{-1}$. For the 2HDM+ a model, we select $m_\chi = 50$ GeV and $\langle\sigma v\rangle = 4.4 \times 10^{-26} \text{ cm}^3 \text{ s}^{-1}$.

We calculate the example spectra in Fig. 16. The spectra analyses are obtained from Ref. [5, 20, 136, 140–143]. We can see that the generated spectra of both the secluded hypercharge model and the 2HDM+ a model are within the envelope of the possible GCE spectra. Due to the large statistical uncertainties of the GCE and the DM profile, we are only able to offer a qualitative comparison and not use the fitting as a quantitative constraint.

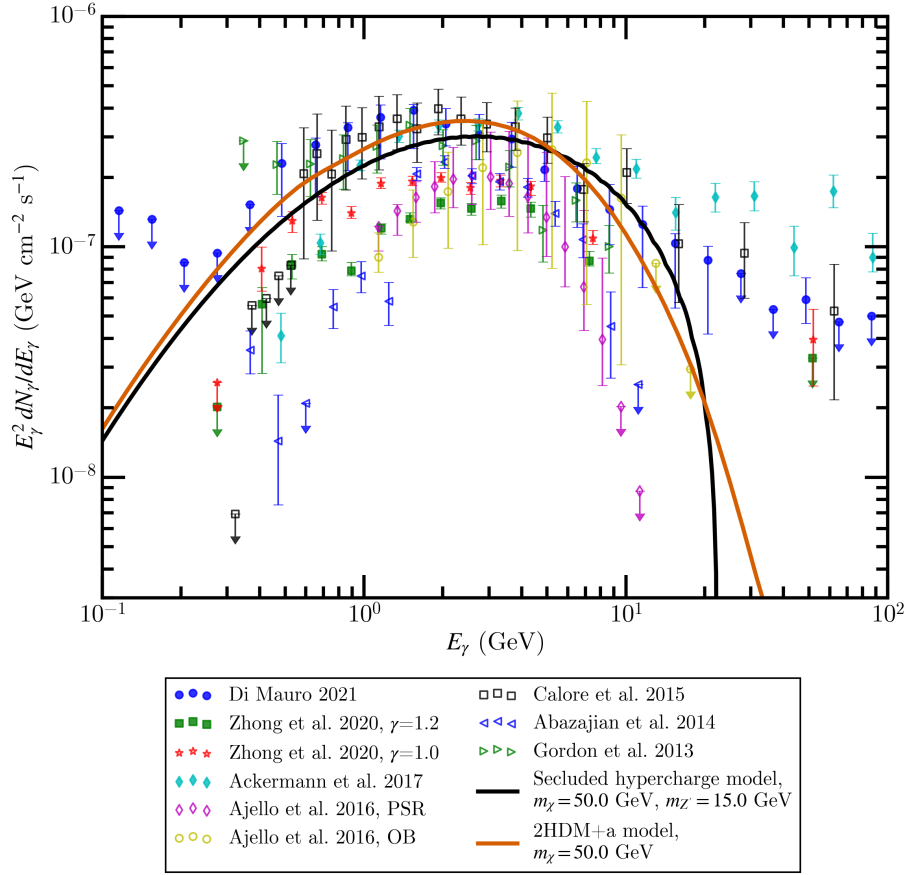


Figure 16. Example spectra of the allowed parameters in our model. The possible GCE spectra with different background models are obtained from [5, 20, 136, 140–143], adapted from [139]. For the secluded hypercharge model, we select $m_\chi = 50$ GeV, $m_{Z'} = 15$ GeV; for the 2HDM+a model, we select $m_\chi = 50$ GeV. The annihilation cross section is at $\langle\sigma v\rangle_{\text{th}} = 4.4 \times 10^{-26} \text{ cm}^3/\text{s}$. The J -factor $J = 1.02 \times 10^{23} \text{ GeV}^2/\text{cm}^5$ using a gNFW profile of $\gamma = 1.25$ and a ROI of $|l| < 20^\circ, 2^\circ < |b| < 20^\circ$.

References

- [1] L. Goodenough and D. Hooper, *Possible Evidence For Dark Matter Annihilation In The Inner Milky Way From The Fermi Gamma Ray Space Telescope*, [0910.2998](#).
- [2] D. Hooper and T.R. Slatyer, *Two Emission Mechanisms in the Fermi Bubbles: A Possible Signal of Annihilating Dark Matter*, *Phys. Dark Univ.* **2** (2013) 118 [[1302.6589](#)].
- [3] T. Daylan, D.P. Finkbeiner, D. Hooper, T. Linden, S.K.N. Portillo, N.L. Rodd et al., *The Characterization of the Gamma-Ray Signal from the Central Milky Way: A Case for Annihilating Dark Matter*, *Phys. Dark Univ.* **12** (2016) 1 [[1402.6703](#)].
- [4] M. Buschmann, N.L. Rodd, B.R. Safdi, L.J. Chang, S. Mishra-Sharma, M. Lisanti et al., *Foreground Mismodeling and the Point Source Explanation of the Fermi Galactic Center Excess*, *Phys. Rev. D* **102** (2020) 023023 [[2002.12373](#)].
- [5] F. Calore, I. Cholis and C. Weniger, *Background Model Systematics for the Fermi GeV*

- Excess*, *JCAP* **03** (2015) 038 [[1409.0042](#)].
- [6] K.N. Abazajian, *The Consistency of Fermi-LAT Observations of the Galactic Center with a Millisecond Pulsar Population in the Central Stellar Cluster*, *JCAP* **03** (2011) 010 [[1011.4275](#)].
 - [7] S.K. Lee, M. Lisanti, B.R. Safdi, T.R. Slatyer and W. Xue, *Evidence for Unresolved γ -Ray Point Sources in the Inner Galaxy*, *Phys. Rev. Lett.* **116** (2016) 051103 [[1506.05124](#)].
 - [8] R. Bartels, S. Krishnamurthy and C. Weniger, *Strong support for the millisecond pulsar origin of the Galactic center GeV excess*, *Phys. Rev. Lett.* **116** (2016) 051102 [[1506.05104](#)].
 - [9] D.V. Malyshev, *Towards resolving the Galactic center GeV excess with millisecond-pulsars-like sources using machine learning*, *Phys. Rev. D* **111** (2025) 043033 [[2401.04565](#)].
 - [10] R.K. Leane and T.R. Slatyer, *Spurious Point Source Signals in the Galactic Center Excess*, *Phys. Rev. Lett.* **125** (2020) 121105 [[2002.12370](#)].
 - [11] R.K. Leane and T.R. Slatyer, *The enigmatic Galactic Center excess: Spurious point sources and signal mismodeling*, *Phys. Rev. D* **102** (2020) 063019 [[2002.12371](#)].
 - [12] F. List, N.L. Rodd, G.F. Lewis and I. Bhat, *The GCE in a New Light: Disentangling the γ -ray Sky with Bayesian Graph Convolutional Neural Networks*, *Phys. Rev. Lett.* **125** (2020) 241102 [[2006.12504](#)].
 - [13] S. Mishra-Sharma and K. Cranmer, *Neural simulation-based inference approach for characterizing the Galactic Center γ -ray excess*, *Phys. Rev. D* **105** (2022) 063017 [[2110.06931](#)].
 - [14] S. Caron, C. Eckner, L. Hendriks, G. Jóhannesson, R. Ruiz de Austri and G. Zaharijas, *Mind the gap: the discrepancy between simulation and reality drives interpretations of the Galactic Center Excess*, *JCAP* **06** (2023) 013 [[2211.09796](#)].
 - [15] F. List, Y. Park, N.L. Rodd, E. Schoen and F. Wolf, *On the Energy Distribution of the Galactic Center Excess' Sources*, [2507.17804](#).
 - [16] O. Macias, C. Gordon, R.M. Crocker, B. Coleman, D. Paterson, S. Horiuchi et al., *Galactic bulge preferred over dark matter for the Galactic centre gamma-ray excess*, *Nature Astron.* **2** (2018) 387 [[1611.06644](#)].
 - [17] R. Bartels, E. Storm, C. Weniger and F. Calore, *The Fermi-LAT GeV excess as a tracer of stellar mass in the Galactic bulge*, *Nature Astron.* **2** (2018) 819 [[1711.04778](#)].
 - [18] O. Macias, S. Horiuchi, M. Kaplinghat, C. Gordon, R.M. Crocker and D.M. Nataf, *Strong Evidence that the Galactic Bulge is Shining in Gamma Rays*, *JCAP* **09** (2019) 042 [[1901.03822](#)].
 - [19] D. Song, C. Eckner, C. Gordon, F. Calore, O. Macias, K.N. Abazajian et al., *Robust inference of the Galactic Centre gamma-ray excess spatial properties*, *Mon. Not. Roy. Astron. Soc.* **530** (2024) 4395 [[2402.05449](#)].
 - [20] M. Di Mauro, *Characteristics of the Galactic Center excess measured with 11 years of Fermi-LAT data*, *Phys. Rev. D* **103** (2021) 063029 [[2101.04694](#)].
 - [21] I. Cholis, Y.-M. Zhong, S.D. McDermott and J.P. Surdutovich, *Return of the templates: Revisiting the Galactic Center excess with multimessenger observations*, *Phys. Rev. D* **105** (2022) 103023 [[2112.09706](#)].

- [22] S.D. McDermott, Y.-M. Zhong and I. Cholis, *On the morphology of the gamma-ray galactic centre excess*, *Mon. Not. Roy. Astron. Soc.* **522** (2023) L21 [[2209.00006](#)].
- [23] Y.-M. Zhong and I. Cholis, *Robustness of the Galactic Center excess morphology against masking*, *Phys. Rev. D* **109** (2024) 123017 [[2401.02481](#)].
- [24] E.D. Ramirez, Y. Sun, M.R. Buckley, S. Mishra-Sharma and T.R. Slatyer, *Inferring the morphology of the Galactic Center excess with Gaussian processes*, *Phys. Rev. D* **111** (2025) 063065 [[2410.21367](#)].
- [25] M.M. Muru, J. Silk, N.I. Libeskind, S. Gottloeber and Y. Hoffman, *Fermi-LAT Galactic Center Excess morphology of dark matter in simulations of the Milky Way galaxy*, [2508.06314](#).
- [26] A. Hussein, L. Necib, M. Kaplinghat, S.Y. Kim, A. Wetzel, J.I. Read et al., *Theoretical Predictions for the Inner Dark Matter Distribution in the Milky Way Informed by Simulations*, [2501.14868](#).
- [27] D. McKeown, *Analysis of shape and angular orientation parameters of velocity-dependent dark matter annihilation signals in Galactic Centers for FIRE simulations*, [2506.16583](#).
- [28] F. Calore, I. Cholis, C. McCabe and C. Weniger, *A Tale of Tails: Dark Matter Interpretations of the Fermi GeV Excess in Light of Background Model Systematics*, *Phys. Rev. D* **91** (2015) 063003 [[1411.4647](#)].
- [29] A. McDaniel, M. Ajello, C.M. Karwin, M. Di Mauro, A. Drlica-Wagner and M.A. Sánchez-Conde, *Legacy analysis of dark matter annihilation from the Milky Way dwarf spheroidal galaxies with 14 years of Fermi-LAT data*, *Phys. Rev. D* **109** (2024) 063024 [[2311.04982](#)].
- [30] P. Agrawal, B. Batell, P.J. Fox and R. Harnik, *WIMPs at the Galactic Center*, *JCAP* **05** (2015) 011 [[1411.2592](#)].
- [31] G. Elor, N.L. Rodd and T.R. Slatyer, *Multistep cascade annihilations of dark matter and the Galactic Center excess*, *Phys. Rev. D* **91** (2015) 103531 [[1503.01773](#)].
- [32] D. Hooper, R.K. Leane, Y.-D. Tsai, S. Wegsman and S.J. Witte, *A systematic study of hidden sector dark matter: application to the gamma-ray and antiproton excesses*, *JHEP* **07** (2020) 163 [[1912.08821](#)].
- [33] M. Carena, J. Osborne, N.R. Shah and C.E.M. Wagner, *Return of the WIMP: Missing energy signals and the Galactic Center excess*, *Phys. Rev. D* **100** (2019) 055002 [[1905.03768](#)].
- [34] J.M. Cline, G. Dupuis, Z. Liu and W. Xue, *The windows for kinetically mixed Z' -mediated dark matter and the galactic center gamma ray excess*, *JHEP* **08** (2014) 131 [[1405.7691](#)].
- [35] A. Berlin, P. Gratia, D. Hooper and S.D. McDermott, *Hidden Sector Dark Matter Models for the Galactic Center Gamma-Ray Excess*, *Phys. Rev. D* **90** (2014) 015032 [[1405.5204](#)].
- [36] A. Berlin, D. Hooper and S.D. McDermott, *Simplified Dark Matter Models for the Galactic Center Gamma-Ray Excess*, *Phys. Rev. D* **89** (2014) 115022 [[1404.0022](#)].
- [37] S. Ipek, D. McKeen and A.E. Nelson, *A Renormalizable Model for the Galactic Center Gamma Ray Excess from Dark Matter Annihilation*, *Phys. Rev. D* **90** (2014) 055021 [[1404.3716](#)].

- [38] A. Martin, J. Shelton and J. Unwin, *Fitting the Galactic Center Gamma-Ray Excess with Cascade Annihilations*, *Phys. Rev. D* **90** (2014) 103513 [[1405.0272](#)].
- [39] E. Izaguirre, G. Krnjaic and B. Shuve, *The Galactic Center Excess from the Bottom Up*, *Phys. Rev. D* **90** (2014) 055002 [[1404.2018](#)].
- [40] J. Liu, N. Weiner and W. Xue, *Signals of a Light Dark Force in the Galactic Center*, *JHEP* **08** (2015) 050 [[1412.1485](#)].
- [41] M. Pospelov, A. Ritz and M.B. Voloshin, *Secluded WIMP Dark Matter*, *Phys. Lett. B* **662** (2008) 53 [[0711.4866](#)].
- [42] LUX collaboration, *First results from the LUX dark matter experiment at the Sanford Underground Research Facility*, *Phys. Rev. Lett.* **112** (2014) 091303 [[1310.8214](#)].
- [43] LZ collaboration, *Dark Matter Search Results from 4.2 Tonne-Years of Exposure of the LUX-ZEPLIN (LZ) Experiment*, [2410.17036](#).
- [44] J.W. Foster, Y. Park, B.R. Safdi, Y. Soreq and W.L. Xu, *Search for dark matter lines at the Galactic Center with 14 years of Fermi data*, *Phys. Rev. D* **107** (2023) 103047 [[2212.07435](#)].
- [45] G. Steigman, B. Dasgupta and J.F. Beacom, *Precise Relic WIMP Abundance and its Impact on Searches for Dark Matter Annihilation*, *Phys. Rev. D* **86** (2012) 023506 [[1204.3622](#)].
- [46] S. Murgia, *The Fermi–LAT Galactic Center Excess: Evidence of Annihilating Dark Matter?*, *Ann. Rev. Nucl. Part. Sci.* **70** (2020) 455.
- [47] M. Abdughani, Y.-Z. Fan, C.-T. Lu, T.-P. Tang and Y.-L.S. Tsai, *Muonphilic dark matter explanation of gamma-ray galactic center excess: a comprehensive analysis*, *JHEP* **07** (2022) 127 [[2111.02946](#)].
- [48] A. Cuoco, B. Eiteneuer, J. Heisig and M. Krämer, *A global fit of the γ -ray galactic center excess within the scalar singlet Higgs portal model*, *JCAP* **06** (2016) 050 [[1603.08228](#)].
- [49] M. Di Mauro and M.W. Winkler, *Multimessenger constraints on the dark matter interpretation of the Fermi-LAT Galactic center excess*, *Phys. Rev. D* **103** (2021) 123005 [[2101.11027](#)].
- [50] M. Kaplinghat, T. Linden and H.-B. Yu, *Galactic Center Excess in γ Rays from Annihilation of Self-Interacting Dark Matter*, *Phys. Rev. Lett.* **114** (2015) 211303 [[1501.03507](#)].
- [51] A. Berlin, J.W. Foster, D. Hooper and G. Krnjaic, *dSphobic Dark Matter*, [2504.12372](#).
- [52] A. Cuoco, M. Krämer and M. Korsmeier, *Novel Dark Matter Constraints from Antiprotons in Light of AMS-02*, *Phys. Rev. Lett.* **118** (2017) 191102 [[1610.03071](#)].
- [53] M.-Y. Cui, Q. Yuan, Y.-L.S. Tsai and Y.-Z. Fan, *Possible dark matter annihilation signal in the AMS-02 antiproton data*, *Phys. Rev. Lett.* **118** (2017) 191101 [[1610.03840](#)].
- [54] I. Cholis, T. Linden and D. Hooper, *A Robust Excess in the Cosmic-Ray Antiproton Spectrum: Implications for Annihilating Dark Matter*, *Phys. Rev. D* **99** (2019) 103026 [[1903.02549](#)].
- [55] M. Boudaud, Y. Génolini, L. Derome, J. Lavalle, D. Maurin, P. Salati et al., *AMS-02 antiprotons’ consistency with a secondary astrophysical origin*, *Phys. Rev. Res.* **2** (2020) 023022 [[1906.07119](#)].

- [56] J. Heisig, M. Korsmeier and M.W. Winkler, *Dark matter or correlated errors: Systematics of the AMS-02 antiproton excess*, *Phys. Rev. Res.* **2** (2020) 043017 [[2005.04237](#)].
- [57] M. Aguilar, L. Ali Cavasonza, G. Ambrosi, L. Arruda, N. Attig, F. Barao et al., *The alpha magnetic spectrometer (ams) on the international space station: Part ii – results from the first seven years*, *Physics Reports* **894** (2021) 1.
- [58] A.E. Egorov and E. Pierpaoli, *Constraints on dark matter annihilation by radio observations of M31*, *Phys. Rev. D* **88** (2013) 023504 [[1304.0517](#)].
- [59] M.H. Chan, *Revisiting the constraints on annihilating dark matter by the radio observational data of M31*, *Phys. Rev. D* **94** (2016) 023507 [[1606.08537](#)].
- [60] A.E. Egorov, *Updated constraints on WIMP dark matter annihilation by radio observations of M31*, *Phys. Rev. D* **106** (2022) 023023 [[2205.01033](#)].
- [61] M.J. Weikert and M.R. Buckley, *Limits on dark matter annihilation from the shape of radio emission in M31*, *JHEP* **02** (2024) 029 [[2303.11354](#)].
- [62] M.H. Chan, C.F. Yeung, L. Cui and C.S. Leung, *Analysing the radio flux density profile of the M31 galaxy: a possible dark matter interpretation*, *Mon. Not. Roy. Astron. Soc.* **501** (2021) 5692 [[2101.00372](#)].
- [63] E.W. Kolb and M.S. Turner, *The Early Universe*, vol. 69 (1990), [10.1201/9780429492860](#).
- [64] J.A. Evans, S. Gori and J. Shelton, *Looking for the WIMP Next Door*, *JHEP* **02** (2018) 100 [[1712.03974](#)].
- [65] A. Alenezi, C. Cesarotti, S. Gori and J. Shelton, *Discovery Prospects for a Minimal Dark Matter Model at Cosmic and Intensity Frontier Experiments*, [2504.00077](#).
- [66] X. Chu, T. Hambye and M.H.G. Tytgat, *The Four Basic Ways of Creating Dark Matter Through a Portal*, *JCAP* **05** (2012) 034 [[1112.0493](#)].
- [67] D. Hooper, *private communication*, .
- [68] J. Koechler and M. Di Mauro, *Leptophilic dark matter in $U(1)_{L_i-L_j}$ models: a solution to the Fermi-LAT Galactic Center Excess consistent with cosmological and laboratory observations*, [2508.02775](#).
- [69] D. Hooper, G. Krnjaic, D. Rocha and S. Roy, *Gamma-Rays and Gravitational Waves from Inelastic Higgs Portal Dark Matter*, [2507.22975](#).
- [70] M. Escudero, S.J. Witte and D. Hooper, *Hidden Sector Dark Matter and the Galactic Center Gamma-Ray Excess: A Closer Look*, *JCAP* **11** (2017) 042 [[1709.07002](#)].
- [71] M. Bauer and T. Plehn, *Yet another introduction to dark matter*, [1705.01987](#).
- [72] G.C. Branco, P.M. Ferreira, L. Lavoura, M.N. Rebelo, M. Sher and J.P. Silva, *Theory and phenomenology of two-Higgs-doublet models*, *Phys. Rept.* **516** (2012) 1 [[1106.0034](#)].
- [73] M.E. Cabrera, J.A. Casas, A. Delgado and S. Robles, *Generalized Blind Spots for Dark Matter Direct Detection in the 2HDM*, *JHEP* **02** (2020) 166 [[1912.01758](#)].
- [74] J.F. Gunion, H.E. Haber, G.L. Kane and S. Dawson, *The Higgs Hunter's Guide*, Westview Press, frontiers in physics ed. (2000).
- [75] S. Weinberg, *The Quantum Theory of Fields, Volume III: Supersymmetry*, Cambridge University Press (2000).

- [76] G. Arcadi, G. Busoni, D. Cabo-Almeida and N. Krishnan, *Is there a scalar or pseudoscalar at 95 GeV?*, *Phys. Rev. D* **110** (2024) 115028 [[2311.14486](#)].
- [77] B. Holdom, *Two $u(1)$'s and epsilon charge shifts*, *Phys. Lett., B* **166** (1986) 196–198.
- [78] H. Ruegg and M. Ruiz-Altaba, *The Stueckelberg field*, *Int. J. Mod. Phys. A* **19** (2004) 3265 [[hep-th/0304245](#)].
- [79] S. Ipek, *Galactic Center Gamma Ray Excess and Higgs Boson(s)*, in *2nd Toyama International Workshop on Higgs as a Probe of New Physics*, 6, 2015 [[1506.00789](#)].
- [80] M. Bauer, U. Haisch and F. Kahlhoefer, *Simplified dark matter models with two Higgs doublets: I. Pseudoscalar mediators*, *JHEP* **05** (2017) 138 [[1701.07427](#)].
- [81] ATLAS collaboration, *Combination and summary of ATLAS dark matter searches interpreted in a 2HDM with a pseudo-scalar mediator using 139 fb⁻¹ of $s=13$ TeV pp collision data*, *Sci. Bull.* **69** (2024) 3005 [[2306.00641](#)].
- [82] LHC DARK MATTER WORKING GROUP collaboration, *LHC Dark Matter Working Group: Next-generation spin-0 dark matter models*, *Phys. Dark Univ.* **27** (2020) 100351 [[1810.09420](#)].
- [83] W. Su, M. White, A.G. Williams and Y. Wu, *Exploring the low $\tan\beta$ region of two Higgs doublet models at the LHC*, *Eur. Phys. J. C* **81** (2021) 810 [[1909.09035](#)].
- [84] LHC HIGGS CROSS SECTION WORKING GROUP collaboration, *Handbook of LHC Higgs Cross Sections: 4. Deciphering the Nature of the Higgs Sector*, [1610.07922](#).
- [85] P.J. Fitzpatrick, H. Liu, T.R. Slatyer and Y.-D. Tsai, *New pathways to the relic abundance of vector-portal dark matter*, *Phys. Rev. D* **106** (2022) 083517 [[2011.01240](#)].
- [86] S. Gori et al., *Dark Sector Physics at High-Intensity Experiments*, [2209.04671](#).
- [87] PLANCK collaboration, *Planck 2018 results. VI. Cosmological parameters*, *Astron. Astrophys.* **641** (2020) A6 [[1807.06209](#)].
- [88] P. Ilten, Y. Soreq, M. Williams and W. Xue, *Serendipity in dark photon searches*, *JHEP* **06** (2018) 004 [[1801.04847](#)].
- [89] T.R. Slatyer, *Indirect dark matter signatures in the cosmic dark ages. I. Generalizing the bound on s -wave dark matter annihilation from Planck results*, *Phys. Rev. D* **93** (2016) 023527 [[1506.03811](#)].
- [90] S. Cassel, *Sommerfeld factor for arbitrary partial wave processes*, *J. Phys. G* **37** (2010) 105009 [[0903.5307](#)].
- [91] S. Tulin, H.-B. Yu and K.M. Zurek, *Beyond Collisionless Dark Matter: Particle Physics Dynamics for Dark Matter Halo Structure*, *Phys. Rev. D* **87** (2013) 115007 [[1302.3898](#)].
- [92] B. Batell, N. Blinov, C. Hearty and R. McGehee, *Exploring Dark Sector Portals with High Intensity Experiments*, in *Snowmass 2021*, 7, 2022 [[2207.06905](#)].
- [93] C.N. Yang, *Selection rules for the dematerialization of a particle into two photons*, *Physical Review* **77** (1950) 242.
- [94] C.B. Jackson, G. Servant, G. Shaughnessy, T.M.P. Tait and M. Taoso, *Higgs in Space!*, *JCAP* **04** (2010) 004 [[0912.0004](#)].
- [95] J. Shelton, S.L. Shapiro and B.D. Fields, *Black hole window into p -wave dark matter annihilation*, *Phys. Rev. Lett.* **115** (2015) 231302 [[1506.04143](#)].

- [96] N.F. Bell, Y. Cai, J.B. Dent, R.K. Leane and T.J. Weiler, *Enhancing Dark Matter Annihilation Rates with Dark Bremsstrahlung*, *Phys. Rev. D* **96** (2017) 023011 [[1705.01105](#)].
- [97] K.R. Dienes, J. Kumar, B. Thomas and D. Yaylali, *Overcoming Velocity Suppression in Dark-Matter Direct-Detection Experiments*, *Phys. Rev. D* **90** (2014) 015012 [[1312.7772](#)].
- [98] T. Abe, M. Fujiwara and J. Hisano, *Loop corrections to dark matter direct detection in a pseudoscalar mediator dark matter model*, *JHEP* **02** (2019) 028 [[1810.01039](#)].
- [99] T. Abe, M. Fujiwara, J. Hisano and Y. Shoji, *Maximum value of the spin-independent cross section in the 2HDM+a*, *JHEP* **01** (2020) 114 [[1910.09771](#)].
- [100] J.R. Ellis, A. Ferstl and K.A. Olive, *Reevaluation of the elastic scattering of supersymmetric dark matter*, *Phys. Lett. B* **481** (2000) 304 [[hep-ph/0001005](#)].
- [101] A. Hektor, L. Marzola and T. Tuvi, *Gamma-ray line constraints on Coy Dark Matter*, *Phys. Rev. D* **95** (2017) 121301 [[1702.02580](#)].
- [102] P. Athron, A. Crivellin, T.E. Gonzalo, S. Iguro and C. Sierra, *Global fit to the 2HDM with generic sources of flavour violation using GAMBIT*, *JHEP* **11** (2024) 133 [[2410.10493](#)].
- [103] W. Skiba and J. Kalinowski, *$B_s \rightarrow \tau^+ \tau^-$ decay in a two Higgs doublet model*, *Nucl. Phys. B* **404** (1993) 3.
- [104] W. Altmannshofer, C. Niehoff and D.M. Straub, *$B_s \rightarrow \mu^+ \mu^-$ as current and future probe of new physics*, *JHEP* **05** (2017) 076 [[1702.05498](#)].
- [105] D. Martinez Santos, *Study of the very rare decay $B_s \rightarrow \mu^+ \mu^-$ in LHCb*, Ph.D. thesis, Santiago de Compostela U., 2010.
- [106] LHCb collaboration, *Measurement of the $B_s^0 \rightarrow \mu^+ \mu^-$ decay properties and search for the $B^0 \rightarrow \mu^+ \mu^-$ and $B_s^0 \rightarrow \mu^+ \mu^- \gamma$ decays*, *Phys. Rev. D* **105** (2022) 012010 [[2108.09283](#)].
- [107] A. Celis, M. Jung, X.-Q. Li and A. Pich, *Sensitivity to charged scalars in $B \rightarrow D^{(*)} \tau \nu_\tau$ and $B \rightarrow \tau \nu_\tau$ decays*, *JHEP* **01** (2013) 054 [[1210.8443](#)].
- [108] A. Crivellin, A. Kokulu and C. Greub, *Flavor-phenomenology of two-Higgs-doublet models with generic Yukawa structure*, *Phys. Rev. D* **87** (2013) 094031 [[1303.5877](#)].
- [109] A. Arbey, F. Mahmoudi, O. Stal and T. Stefaniak, *Status of the Charged Higgs Boson in Two Higgs Doublet Models*, *Eur. Phys. J. C* **78** (2018) 182 [[1706.07414](#)].
- [110] ATLAS collaboration, *Combination of searches for invisible decays of the Higgs boson using 139 fb⁻¹ of proton-proton collision data at $s=13$ TeV collected with the ATLAS experiment*, *Phys. Lett. B* **842** (2023) 137963 [[2301.10731](#)].
- [111] A. Coogan, L. Morrison and S. Profumo, *Hazma: A Python Toolkit for Studying Indirect Detection of Sub-GeV Dark Matter*, [1907.11846](#).
- [112] J. Alwall, R. Frederix, S. Frixione, V. Hirschi, F. Maltoni, O. Mattelaer et al., *The automated computation of tree-level and next-to-leading order differential cross sections, and their matching to parton shower simulations*, *JHEP* **07** (2014) 079 [[1405.0301](#)].
- [113] NNPDF collaboration, *Parton distributions with QED corrections*, *Nucl. Phys. B* **877** (2013) 290 [[1308.0598](#)].
- [114] A. Buckley, J. Ferrando, S. Lloyd, K. Nordström, B. Page, M. Rüfenacht et al., *LHAPDF6: parton density access in the LHC precision era*, *Eur. Phys. J. C* **75** (2015) 132 [[1412.7420](#)].

- [115] C. Bierlich et al., *A comprehensive guide to the physics and usage of PYTHIA 8.3*, *SciPost Phys. Codeb.* **2022** (2022) 8 [[2203.11601](#)].
- [116] DELPHES 3 collaboration, *DELPHES 3, A modular framework for fast simulation of a generic collider experiment*, *JHEP* **02** (2014) 057 [[1307.6346](#)].
- [117] M. Cacciari, G.P. Salam and G. Soyez, *FastJet User Manual*, *Eur. Phys. J. C* **72** (2012) 1896 [[1111.6097](#)].
- [118] ATLAS collaboration, *Search for associated production of a Z boson with an invisibly decaying Higgs boson or dark matter candidates at $s=13$ TeV with the ATLAS detector*, *Phys. Lett. B* **829** (2022) 137066 [[2111.08372](#)].
- [119] ATLAS collaboration, *Search for invisible Higgs-boson decays in events with vector-boson fusion signatures using 139 fb^{-1} of proton-proton data recorded by the ATLAS experiment*, *JHEP* **08** (2022) 104 [[2202.07953](#)].
- [120] ATLAS collaboration, *Search for dark matter produced in association with a Standard Model Higgs boson decaying into b-quarks using the full Run 2 dataset from the ATLAS detector*, *JHEP* **11** (2021) 209 [[2108.13391](#)].
- [121] J.N. Guenther, *Overview of the QCD phase diagram: Recent progress from the lattice*, *Eur. Phys. J. A* **57** (2021) 136 [[2010.15503](#)].
- [122] J. Billard et al., *Direct detection of dark matter—APPEC committee report**, *Rept. Prog. Phys.* **85** (2022) 056201 [[2104.07634](#)].
- [123] DARWIN collaboration, *DARWIN: towards the ultimate dark matter detector*, *JCAP* **11** (2016) 017 [[1606.07001](#)].
- [124] XLZD collaboration, *The XLZD Design Book: Towards the Next-Generation Liquid Xenon Observatory for Dark Matter and Neutrino Physics*, [2410.17137](#).
- [125] SHiP collaboration, *The SHiP experiment at the proposed CERN SPS Beam Dump Facility*, *Eur. Phys. J. C* **82** (2022) 486 [[2112.01487](#)].
- [126] G. Apollinari, I. Béjar Alonso, O. Brüning, M. Lamont and L. Rossi, *High-luminosity large hadron collider (hl-lhc): Preliminary design report*, Tech. Rep. [CERN-2015-005](#), CERN, Geneva (2015), [DOI](#).
- [127] ATLAS Collaboration, *Updated projections for $B_{(s)}^0 \rightarrow \mu^+ \mu^-$ measurements with the atlas detector at the hl-lhc*, ATLAS Public Note [ATL-PHYS-PUB-2025-016](#), CERN, Geneva (March, 2025).
- [128] M. Cepeda et al., *Report from Working Group 2: Higgs Physics at the HL-LHC and HE-LHC*, *CERN Yellow Rep. Monogr.* **7** (2019) 221 [[1902.00134](#)].
- [129] CTAO collaboration, *Dark matter line searches with the Cherenkov Telescope Array*, *JCAP* **07** (2024) 047 [[2403.04857](#)].
- [130] APT collaboration, *The Advanced Particle-astrophysics Telescope (APT) Project Status*, *PoS ICRC2021* (2021) 655.
- [131] S. Alnussirat et al., *The Advanced Particle-astrophysics Telescope: Simulation of the Instrument Performance for Gamma-Ray Detection*, *PoS ICRC2021* (2021) 590.
- [132] F. Xu and D. Hooper, *Dark matter discovery potential of the Advanced Particle-Astrophysics Telescope*, *Phys. Rev. D* **109** (2024) 083032 [[2308.15538](#)].

- [133] D. Alonso-González, D. Cerdeño, P. Foldenauer and J.M. No, *GeV-scale thermal dark matter from dark photons: tightly constrained, yet allowed*, [2507.11376](#).
- [134] M. Cirelli, G. Corcella, A. Hektor, G. Hutsi, M. Kadastik, P. Panci et al., *PPPC 4 DM ID: A Poor Particle Physicist Cookbook for Dark Matter Indirect Detection*, *JCAP* **03** (2011) 051 [[1012.4515](#)].
- [135] P. Ciafaloni, D. Comelli, A. Riotto, F. Sala, A. Strumia and A. Urbano, *Weak Corrections are Relevant for Dark Matter Indirect Detection*, *JCAP* **03** (2011) 019 [[1009.0224](#)].
- [136] FERMI-LAT collaboration, *The Fermi Galactic Center GeV Excess and Implications for Dark Matter*, *Astrophys. J.* **840** (2017) 43 [[1704.03910](#)].
- [137] L. Bergström, P. Ullio and J.H. Buckley, *Observability of γ rays from dark matter neutralino annihilations in the milky way halo*, *Astroparticle Physics* **9** (1998) 137.
- [138] J.F. Navarro, C.S. Frenk and S.D.M. White, *A Universal density profile from hierarchical clustering*, *Astrophys. J.* **490** (1997) 493 [[astro-ph/9611107](#)].
- [139] J.T. Dinsmore and T.R. Slatyer, *Luminosity functions consistent with a pulsar-dominated Galactic Center excess*, *JCAP* **06** (2022) 025 [[2112.09699](#)].
- [140] Y.-M. Zhong, S.D. McDermott, I. Cholis and P.J. Fox, *Testing the Sensitivity of the Galactic Center Excess to the Point Source Mask*, *Phys. Rev. Lett.* **124** (2020) 231103 [[1911.12369](#)].
- [141] C. Gordon and O. Macias, *Dark Matter and Pulsar Model Constraints from Galactic Center Fermi-LAT Gamma Ray Observations*, *Phys. Rev. D* **88** (2013) 083521 [[1306.5725](#)].
- [142] FERMI-LAT collaboration, *Fermi-LAT Observations of High-Energy γ -Ray Emission Toward the Galactic Center*, *Astrophys. J.* **819** (2016) 44 [[1511.02938](#)].
- [143] K.N. Abazajian, N. Canac, S. Horiuchi and M. Kaplinghat, *Astrophysical and Dark Matter Interpretations of Extended Gamma-Ray Emission from the Galactic Center*, *Phys. Rev. D* **90** (2014) 023526 [[1402.4090](#)].